The Environment and Climate Change Canada Carbon Assimilation System (EC-CAS v1.0) : demonstration with simulated CO observations

Vikram Khade[1,2], Saroja M. Polavarapu[1,2], Michael Neish[1], Pieter L. Houtekamer[3], Dylan B.A. Jones[2], Seung-Jong Baek[3], Tai-Long He[2], and Sylvie Gravel[3]

[1]Environment and Climate Change Canada, 4905 Dufferin Street, Toronto, Ontario, Canada, M3H 5T4
[2]Department of Physics, University of Toronto, 60 St. George Street, Toronto, Ontario, Canada, M5S 1A7
[3]Environment and Climate Change Canada, 2121 route Transcanadienne, Dorval, Quebec, Canada, H9P 1J3

Correspondence: Vikram Khade (vikram.khade@canada.ca)

Abstract. In this study, we present the development of a new coupled weather and CO data assimilation system based on Environment and Climate Change Canada's (ECCC's) operational Ensemble Kalman Filter (EnKF). The estimated meteorological state is augmented to include carbon monoxide (CO). Variable localization is used to prevent the direct update of meteorology by the observations of the constituents and vice versa. Physical localization is used to damp spurious analysis increments far from a given observation. Perturbed surface flux fields are used to account for the uncertainty in CO due to errors in the surface fluxes. The system is demonstrated for the estimation of 3-dimensional CO states using simulated observations from a variety of networks. First, a hypothetically dense, uniformly distributed observation network is used to demonstrate that the system is working. More realistic observation networks based on surface hourly observations, and space-based observations provide a demonstration of the complementarity of the different networks and further confirm the reasonable behaviour of the coupled assimilation system. Having demonstrated the ability to estimate CO distributions, this system will be extended to estimate surface fluxes in the future.

1 Introduction

Environment and Climate Change Canada (ECCC) operates a greenhouse gases (GHG) measurement network which has seen rapid expansion during the past decade. ECCC also possesses a GHG inventory reporting division. As required by United Nations Framework on Climate Change (UNFCCC) commitments, Canadian emissions are quantified and reported using bottom-up methods (NIR 2019, http://www.publications.gc.ca/site/eng/9.506002/publication.html). In order to assess the national impact of mitigation efforts, knowledge of the natural sources and sinks is also needed. The challenge is that there are huge uncertainties in the natural carbon budget for Canada. For example, Crowell et al. (2019) find a range of uncertainty estimates of Boreal North American (which is primarily Canada plus Alaska) surface fluxes from 480 to 700 TgC yr^{-1} for an ensemble of inversion results for 2015 and 2016. This uncertainty in the biospheric uptake is comparable to the NIR estimate of anthropogenic emissions (568 and 559 TgC yr^{-1} for 2015 and 2016 respectively) for Canada (NIR, 2019). In addition, there is much unknown about the fate of carbon stored in the permafrost under a warming climate (Voigt et al., 2019), and this will have implications for the global as well as the Canadian carbon budget. Thus, ECCC has a need to better understand and quantify GHG sources and sinks on the national scale. The ECCC Carbon Assimilation System (EC-CAS) was proposed to address these needs using the available tools, namely, operational atmospheric modelling and assimilation systems. The eventual goal of EC-CAS is to characterize CO_2, CO and CH_4 distributions and surface fluxes both globally and over Canada with a focus on the natural carbon cycle. An important aspect of the impact of climate change on boreal forests is the influence of wildfires on the carbon balance in these regions. Over the past several decades there has been an increase in the frequency of wildfires and this trend is expected to continue (Abatzoglou and Williams, 2016; Flannigan et al., 2009), which will have a significant impact on the Canadian carbon budget and on the Canadian economy. In addition, as a combustion tracer, observations of CO can provide constraints on CO_2 emissions from fires and help discriminate between combustion-related CO_2 fluxes and fluxes from terrestrial biosphere (Palmer et al., 2003; Wang et. al., 2009; van der Laan-Luijkx et al., 2015). It is for this reason that EC-CAS also includes CO alongside the greenhouse gases CO_2 and CH_4. EC-CAS will be a significant undertaking and only the very first step toward this system is described here, namely, the estimation of 3D CO distributions. Of the three species of interest, we chose to start with the CO because of its shorter lifetime of about 2 months. Thus, the computational cost to test the new system could be minimized.

Carbon Monoxide (CO) plays a role in both tropospheric chemistry and in climate. In terms of air quality, CO is an important precursor of tropospheric ozone, but it is also a by-product of incomplete combustion and thus correlates well with anthropogenic sources of greenhouse gases from fossil fuel and biofuel burning and from forest fires. CO has a lifetime of 1-2 months which is in-between the air quality and climate timescales and thus data assimilation systems (DAS) that assimilate CO can focus on either the air quality or the climate problem. Tropospheric atmospheric composition prediction concerns short time scales (forecasts up to 5 days) whereas climate problems concern the estimation of surface fluxes over months to years. Data assimilation systems whose primary objective is to better understand and predict tropospheric pollution typically use a coupled weather and chemistry model with short assimilation windows (e.g. 12 h) to initiate short forecasts. The CO

observations are used to estimate CO initial states for the forecasts with either an Ensemble Kalman Filter (EnKF) (Barré et al., 2015; Miyazaki et al., 2012) or a 4-d Variational (4D-Var) approach (Inness et al., 2019, 2015). The chemistry model typically includes the numerous gas phase and aerosol reactions relevant for air quality. On the other hand, systems focused on CO's influence on climate are typically "inversion systems" wherein observations of CO concentrations are used to estimate CO surface fluxes. Here again, both ensemble (Miyazaki et al., 2015, 2012) and variational (Jiang et al., 2017, 2015a, b, 2013, 2011; Fortems-Cheiney et al., 2011) approaches have been used. Typically a chemistry transport model (CTM) driven by offline meteorological analyses is used. Simplified chemistry models with monthly hydroxide (OH) fields (Yin et al., 2015; Fortems-Cheiney et al., 2011; Jiang et al., 2017, 2015a, b, 2013, 2011) or full tropospheric chemistry models (Miyazaki et al., 2015, 2012) may be used.

EC-CAS v1.0 adapts the operational Ensemble Kalman Filter (EnKF) (Houtekamer et al., 2014) to perform a coupled meteorology and CO state estimation as in Barré et al. (2015) and Gaubert et al. (2016). With this choice, EC-CAS v1.0 can directly simulate and account for all components of transport error (i.e. errors arising from model formulation, meteorological state, constituent initial conditions) as well as observation and surface flux errors. See Polavarapu et al. (2016) for a detailed discussion of transport errors. EC-CAS will also be able to handle the vast quantities of observations that are anticipated since currently, roughly 10^6 observations are already assimilated every day for weather forecasts.

In the present paper we introduce the first version of EC-CAS to demonstrate the extension of the ensemble Kalman filter (Houtekamer et al., 2014) to estimate CO atmospheric distributions. To demonstrate that the system is working, 3-dimensional CO fields are estimated by assimilating observations from four different networks. The outline of the paper is as follows. Section 2 describes the various components of EC-CAS system. Section 3 presents the experimental design while section 4 describes the data assimilation (DA) experiments and their results. Section 5 presents the conclusions of this work and delineates planned future developments of EC-CAS.

2 System description and development

2.1 EC-CAS

The EC-CAS system consists of a coupled weather and constituent transport model as the forecast model and an Ensemble Kalman filter (EnKF) as the data assimilation technique. Figure 1 shows a schematic overview of EC-CAS. A number ($N = 64$) of 6 h model forecasts are simultaneously integrated from N meteorological and CO initial conditions with forcing from N perturbed CO surface fluxes. The spread of 6 h ensemble forecasts about their mean is used at each data assimilation (DA) cycle to define the forecast error covariance. The EnKF is used to optimally combine the forecast fields with the observations using both the forecast and observation error covariance matrices to produce the analysis ensemble at each DA cycle. The optimality here refers to the fact that the solution minimizes the analysis error variance if the uncertainty estimates of the

observations (including representation errors) and the ensemble mean forecast as represented by their corresponding error
80 covariance matrices are correctly specified and if errors are Gaussian. Thus, a key component in the analysis step is the
forecast error uncertainty estimate which is estimated by the N ensemble forecasts in this algorithm. This permits a temporally
evolving and flow dependent specification of forecast errors.

2.2 The forecast model

The forecast model used in EC-CAS is called GEM-MACH-GHG (Polavarapu et al., 2016; Neish et al., 2019). This model
85 is a variant of GEM (Global Environmental Multiscale), ECCC's operational weather forecast model (Côté et al., 1998a, b;
Girard et al., 2014) that was developed for the simulation of greenhouse gases. A detailed description of the GEM-MACH-
GHG model is found in Polavarapu et al. (2016), so only a few salient points are mentioned here along with recent model
updates. Compared to the operational global weather forecast model, GEM-MACH-GHG uses a lower resolution with $0.9°$
grid spacing in both latitude and longitude but the same 80 vertical levels from the surface to 0.1 hPa. The vertical coordinate is
90 a type of hybrid terrain-following coordinate (Girard et al., 2014). The advection scheme uses a semi-Lagrangian approach for
both meteorology and tracers. Modifications were implemented to conserve tracer mass on the global scale (see Polavarapu
et al. (2016)). This included defining tracer variables as dry mole fractions. In addition, tracers are transported through the
Kain-Fritsch deep convection scheme (Kain and Fritsch, 1990; Kain, 2004) but not through a shallow convection scheme. The
boundary layer scheme uses a prognostic turbulent kinetic energy (TKE) equation to specify the thermal eddy diffusivity (see
95 McTaggart-Cowan and Zadra (2015)). In Polavarapu et al. (2016, 2018), it was necessary to impose a minimum diffusivity of
$10 \text{ m}^2\text{s}^{-1}$ in the boundary layer. However, recent model improvements enabled the minimum diffusivity to be lowered to 1
m^2s^{-1} as in Kim et al. (2020).

An operational air quality forecast model based on GEM is used to produce 48 h forecasts of air quality health index on a
limited area domain covering most of North America. This model is called GEM-MACH (Anselmo et al., 2010; Gong et al.,
100 2015; Pavlovic et al., 2016) and it employs moderately detailed parameterizations of tropospheric chemistry using 42 gas-
phase species, 20 aqueous-phase species, and nine aerosol chemical components. In contrast, GEM-MACH-GHG uses simple
parameterized chemistry for CH_4 and CO while CO_2 is treated as a passive tracer. Thus, GEM-MACH-GHG could be used
for multi-year simulations and surface flux estimations of long-lived constituents with an EnKF. The computational expense
of complete chemistry would be prohibitive and difficult to justify for a system focused on carbon fluxes. However, other
105 model processes from GEM-MACH are used in GEM-MACH-GHG, namely, the vertical diffusion and emissions injection.
In GEM-MACH-GHG, the methane (CH_4) parameterization involves a single loss rate with a monthly [OH] climatology. The
rate constant is specified following the JPL (2011) formulation for bimolecular reaction for methane (see their page 1-12).
The parameterized chemistry model used for CO is identical to that used in GEOS-Chem (http://geos-chem.org) in that CO
destruction is parameterized following JPL (2011). The same [OH] climatology is used for CH_4 and CO. Specifically, the

110   [OH] monthly climatology is from Spivakovsky et al. (2000) regridded to GEM-MACH-GHG's grid. The production of CO from CH_4 is computed assuming each methane molecule destroyed becomes a CO molecule.

For the CH_4 simulation, the surface fluxes were obtained from CT-CH_4 (Bruhwiler et al., 2014). Since CT-CH_4 surface fluxes are available from 2000-2010, the last 5-year mean (2006-2010) fluxes were used for the 2015 EC-CAS simulation. The initial condition (IC) for CH_4 for 1 January 2015 was approximated with the CH_4 atmospheric mole fractions from CT-CH_4 at the

115   end of 2010 plus a globally uniform offset to account for the increase in CH_4 from 2010 to 2015 (30 ppb, estimated based on the difference from observations at the South Pole). Even though the initial condition is not correct, the impact of the errors in the CH_4 initial condition (the synoptic spatial patterns) dissipates within weeks. These prescribed CH_4 surface fluxes and initial conditions appear reasonable as the model simulated CH_4 compares well with surface observations.

To define the CO initial state, an inversion constrained by space based observations from MOPITT (Measurement of Pollution

120   in the Troposphere) instrument v7J (Drummond, 1992) was performed with GEOS-Chem on a $4° \times 5°$ grid. The CO combustion emissions are from Hemispheric Transport of Air Pollutants (http://www.htap.org) (Janssens-Maenhout et al., 2015). Biogenic emissions of isoprene, methanol, acetone, and monoterpenes are from a GEM-MACH simulation, with an assumed yield of CO from the oxidation of these hydrocarbons that is based on the GEOS-Chem CO-only simulation employed in Kopacz et al. (2010) and Jiang et al. (2011, 2015a, 2017). The monthly CO posterior surface fluxes obtained for December 2014 and

125   throughout 2015 were used in EC-CAS EnKF cycles. Since GEOS-Chem is widely used for assimilation of MOPITT CO data, we use a posterior CO distribution from GEOS-Chem for 1 December 2014 18:00:00 UTC as the initial state on 27 December 2014 18:00:00 UTC.

2.3   The Ensemble Kalman Filter used for weather forecasting

ECCC has been developing an ensemble Kalman Filter (EnKF) for medium range weather prediction since the mid 1990's

130   (Houtekamer et. al., 1996). In 2005, ECCC became the first to implement an EnKF for operational global weather forecasting (Houtekamer and Mitchell, 2005). As an operational system, ECCC's EnKF is constantly evolving and improving. However, in order to implement the extensions for CO assimilation described in this article, it was necessary to freeze a version. Thus our EnKF branches off from the Global Ensemble Prediction System (GEPS) version 4.1.1 which was implemented operationally on 15 December 2015 and described in Houtekamer et al. (2014). The history of changes to the operational GEPS is available

135   at https://eccc-msc.github.io/open-data/msc-data/nwp_geps/readme_geps_en/. The history is also discussed in Houtekamer et al. (2014). The current operational version is described in Houtekamer et al. (2019).

There are multiple ways to formulate an EnKF. The GEPS algorithm uses a so-called stochastic formulation (Lawson and Hansen, 2004) in which each ensemble member assimilates a different set of observations. The observation sets are obtained by perturbing the actual observations with realizations from the prescribed observation error covariance matrix. This formulation

140   may have an advantage when dealing with nonlinear error growth (Lawson and Hansen, 2004). Though the EnKF equations

have been defined numerous times before, we present the equations here as some readers may be more familiar with chemistry-transport model applications.

The Kalman Filter equation (Ghil et al., 1981; Cohn and Parrish, 1991) at a particular DA cycle at time t is given by,

$$\mathbf{x}^a(t) \;\; = \;\; \mathbf{x}^f(t) \;+\; \mathbf{P}^f(t)\mathbf{H}^T(t)\,[\mathbf{H}(t)\mathbf{P}^f(t)\mathbf{H}^T(t) + \mathbf{R}(t)]^{-1}\,(\mathbf{y}^o(t) - \mathbf{H}(t)\mathbf{x}^f(t)) \tag{1}$$

$\mathbf{x}^f$ is the forecast field produced by a 6 h forecast of GEM-MACH. $\mathbf{x}^a$ is the analysis produced by combining the information content in the forecast fields and the observations. $\mathbf{H}$ is the observation operator which maps the model state to the observation space. $\mathbf{P}^f(t)$ is the forecast error covariance matrix. $\mathbf{y}^o$ is the observation vector of dimension m and matrix $\mathbf{R}$ of dimension $m\times m$ represents the error in $\mathbf{y}^o$. In Eq. (1), $\mathbf{x}^f$ and $\mathbf{x}^a$ are state vectors of dimension $d = 400\times200\times(80\times4+2)$. The dimensionality of the model grid is 400×200. The number of vertical levels is 80. There are four 3-dimensional meteorological variables, namely temperature, two horizontal components of winds and the natural logarithm of specific humidity. In addition, the state vector includes the 2-dimensional fields of surface pressure and radiative temperature at the surface. With the ensemble approach, the forecast error covariance, $\mathbf{P}^f(t)$ need not be computed explicitly. Instead, the terms in Eq. 1 involving $\mathbf{P}^f(t)$ are computed as follows,

$$\mathbf{P}^f\mathbf{H}^T \;\; = \;\; \frac{1}{(N-1)}\sum_{i=1}^{N}(x_i^f - \overline{x^f})(\mathbf{H}x_i^f - \overline{\mathbf{H}x^f})^T \tag{2}$$

$$\mathbf{H}\mathbf{P}^f\mathbf{H}^T \;\; = \;\; \frac{1}{(N-1)}\sum_{i=1}^{N}(\mathbf{H}x_i^f - \overline{\mathbf{H}x^f})(\mathbf{H}x_i^f - \overline{\mathbf{H}x^f})^T \tag{3}$$

where $\overline{x^f}$ and $\overline{\mathbf{H}x^f}$ are the ensemble means. The t in the parenthesis is dropped for readability. The summation is over the ensemble members.

The quantity,

$$\mathbf{K}(t) \;\; = \;\; \mathbf{P}^f\mathbf{H}^T\,[\mathbf{H}\mathbf{P}^f\mathbf{H}^T + \mathbf{R}]^{-1} \tag{4}$$

in Eq. (1) is known as the Kalman gain, where the t in the parenthesis for quantities on the right side are dropped for readability. $(\mathbf{H}\mathbf{P}^f\mathbf{H}^T + \mathbf{R})$ can be a huge matrix (order $\approx 10^6$) (Houtekamer et al., 2019) and its inversion is computationally onerous. This problem is circumvented by solving this equation *sequentially* (Cohn and Parrish, 1991; Anderson, 2001; Houtekamer and Mitchell, 2001). In sequential processing, the total number of observations m are subdivided into N_b subsets, known as *batches* containing at most p observations each.

Then, the assimilation proceeds as follows :

$$\mathbf{x}_1^a(t) \;=\; \mathbf{x}^f(t) + \mathbf{P}^f\mathbf{H}_1^T[\mathbf{H}_1\mathbf{P}^f\mathbf{H}_1^T + \mathbf{R}_1]^{-1}(\mathbf{y}_1^o - \mathbf{H}_1\mathbf{x}^f) \qquad \textit{Pass 1}$$

$$\mathbf{x}_2^a(t) \;=\; \mathbf{x}_1^a(t) + \mathbf{P}^f\mathbf{H}_2^T[\mathbf{H}_2\mathbf{P}^f\mathbf{H}_2^T + \mathbf{R}_2]^{-1}(\mathbf{y}_2^o - \mathbf{H}_2\mathbf{x}_1^a) \qquad \textit{Pass 2}$$

$$\vdots$$

$$\mathbf{x}_{N_b}^a(t) \;=\; \mathbf{x}_{N_b-1}^a(t) + \mathbf{P}^f\mathbf{H}_{N_b}^T[\mathbf{H}_{N_b}\mathbf{P}^f\mathbf{H}_{N_b}^T + \mathbf{R}_{N_b}]^{-1}(\mathbf{y}_{N_b}^o - \mathbf{H}_{N_b}\mathbf{x}_{N_b-1}^a) \qquad \textit{Pass } N_b$$

The subscripts $1, 2, ..., N_b$ represent the pass numbers. $\mathbf{x}_{N_b}^a(t)$ is the updated state (as if all the observations were processed simultaneously). The analysis from a given pass is used as the forecast field in the next pass. At each pass at most 600 observations are assimilated.

Though the covariance estimate $\mathbf{P}^f$ obtained from the ensemble is state dependent, owing to the small size of the ensemble, this estimate is noisy. This is remedied by the use of physical localization. The Kalman gain in Eq. (4) is modified as,

$$\mathbf{K}(t) \;=\; (\rho_\mathbf{m} \circ (\mathbf{P}^f\mathbf{H}^T))\;[\rho_\mathbf{o} \circ (\mathbf{H}\mathbf{P}^f\mathbf{H}^T) + \mathbf{R}]^{-1} \qquad\qquad (5)$$

where $\rho_\mathbf{m}$ and $\rho_\mathbf{o}$ constitute the physical localization in the model space and observation space, respectively and $\circ$ denotes the Hadamard product. These matrices contain weights that smoothly decrease towards zero as the distance from the observation increases. The localization in the model space ($\rho_\mathbf{m}$) requires the distance between observations and model coordinates while the localization in the observation space ($\rho_\mathbf{o}$) requires the distance between observations (Houtekamer et al., 2016). The co-variances in $\mathbf{P}^f\mathbf{H}^T$ are multiplied elementwise by $\rho_\mathbf{m}$. Similarly, the covariances in $\mathbf{H}\mathbf{P}^f\mathbf{H}^T$ are multiplied elementwise by $\rho_\mathbf{o}$. The ensemble size is typically much smaller than the dimensionality of the model. For example, in this work the ensemble size is 64 while the model dimensionality is $\approx 10^7$. Consequently, the correlation estimate calculated from the ensemble can be spurious. Localization is designed to ameliorate this problem of spurious correlations (Hamill et al., 2001). The rate of decrease of the weight is dictated by the Gaspari-Cohn function (Gaspari and Cohn, 1999; Houtekamer and Mitchell, 2001). The localization radii for meteorological variables are the same as those given in Table 3 of Houtekamer et al. (2014). The batches of observations are created within four vertical layers and the localization radius increased with the height of the layer, ranging from 2100 km for the lowest layer (1050-400 hPA) to 3000 km for the highest layer (14-2 hPa).

To simulate model errors, the GEPS 4.1.1 uses different model parameters for different forecast ensemble members. These parameters are associated with the most uncertain parameterized physical processes such as boundary layer turbulence and deep convection (Table S1). Each ensemble member is assigned a unique combination of optional values. The GEPS 4.1.1 also uses an additive homogeneous, isotropic climatological error produced using the so-called NMC method (Parrish and Derber, 1992; Bannister, 2008) for additional model error simulation (Houtekamer et al., 2019).

Some features of later implementations of GEPS were also incorporated in EC-CAS. During the forecasting step, an Incremental Analysis Updating (IAU) scheme (Bloom et al., 1996; Houtekamer et al., 2019) from GEPS 5.0.0 is applied to control high frequency waves generated by analysis insertion during the ensemble forecasts. GEPS 5.0.0 is detailed at the Meteorological Service of Canada's Open Data site (https://eccc-msc.github.io/open-data/msc-data/nwp_geps/changelog_geps_en/).

A few more changes were made specifically for EC-CAS. First, the horizontal resolution was coarsened to $0.9°$ (400×200 grid points in a uniformly spaced latitude-longitude grid). Second, the number of ensemble members was reduced from 256 to 64. Third, satellite radiances were removed from the types of meteorological data to be assimilated. Thus EC-CAS assimilates radiosonde, surface (from ships and land sites), aircraft, scatterometer, cloud-drift winds and GPS radio occultation observations. The first two changes were needed for computational efficiency during model development and testing. The impact of all three changes is shown in section 1 of the supplemental material. Figures S1 to S4 compare statistics (bias and standard deviation) of observation minus model differences for radiosondes at 00 and 12 UTC for zonal wind, meridional wind, temperature and dewpoint depression. As expected, our system has degraded performance relative the full system, most notably for error standard deviation for wind components. Other EnKF systems for CO data assimilation use 30 members (Gaubert et al., 2016; Barré et al., 2015; Miyazaki et al., 2015). Increases in ensemble size are envisioned in the future. The reason for not assimilating satellite radiances is evident from Figures S5 and S6. Scores for wind components and temperature in the stratosphere are actually better without these observations. Radiance assimilation is challenging in the stratosphere due to a combination of factors : the covariance localization in a region with long horizontal correlation length, dense observations and the use of a sequential algorithm (Houtekamer et al., 2016). Although moisture in the troposphere is degraded without radiance assimilation, we preferred to retain the improved performance of the wind fields, particularly in the tropics (Figure S6). Interestingly, the CO EnKF systems of Barré et al. (2015) and Gaubert et al. (2016) also do not assimilate satellite radiance measurements.

2.4 EnKF extensions for CO data assimilation

The state vector discussed in section 2.3 is augmented to include the CO field. Variable localization (Kang et al., 2011) is implemented in the EnKF code by modifying Eq. (5) as follows.

$$\mathbf{K}(t) \quad = \quad (\rho_{\mathbf{m}}^{\mathbf{v}} \circ \rho_{\mathbf{m}} \circ (\mathbf{P}^f \mathbf{H}^T)) \ [\rho_{\mathbf{o}}^{\mathbf{v}} \circ \rho_{\mathbf{o}} \circ (\mathbf{H}\mathbf{P}^f \mathbf{H}^T) + \mathbf{R}]^{-1} \tag{6}$$

Each element of $\rho_{\mathbf{m}}^{\mathbf{v}}$ and $\rho_{\mathbf{o}}^{\mathbf{v}}$ is either 1 or 0. Unlike the physical localization matrices, the elements of variable localization matrices are not distant dependent; they are rather *variable type* dependent. A given element is 1 if the row and column variable is of the same type and 0 otherwise. The (i, j) th element of $\rho_{\mathbf{m}}^{\mathbf{v}}$ and $\rho_{\mathbf{o}}^{\mathbf{v}}$ is set to one if one desires an observation of the jth variable to impact the update of ith variable. Setting the (i, j) th element to zero ensures that the observation of the jth variable does not contribute to the update of the ith variable. For example, if both, the row and column of $\mathbf{H}\mathbf{P}^f \mathbf{H}^T$ correspond to a CO

observation, the respective element of $\rho_\mathbf{o}^\mathbf{v}$ is set to 1. In our initial implementation of EC-CAS, presented in this work, variable localization is implemented such that meteorological observations do not directly update CO state and CO observations do not update the meteorological state as in Inness et al. (2015), Barré et al. (2015) and Gaubert et al. (2016). Since Miyazaki et al. (2011) and Kang et al. (2011) show that CO_2 updates through wind observations are beneficial, this issue will be considered in future EC-CAS developments. It is worth noting that it is still possible for the CO state to indirectly improve due to the assimilation of wind observations. This can occur because improvement in winds due to meteorological observations leads to an improvement in the spatial distribution of CO. An important tuning parameter of the EnKF is the localization radius. Various localization radii for CO forecast error covariances were tried. Values of 2000 km in the horizontal and 4 km in the vertical gave the best results. The EnKF code with the extensions developed here is available in Khade et al. (2020).

3 Experimental Design

The current paper describes the experiments run for the development and testing of state estimation of CO using simulated observations. The ultimate goal is to develop a system that ingests real GHG observations. However, testing of the system using simulated observations is an important milestone. It not only demonstrates that the system is working properly but also illustrates and defines errors achievable in the best case scenario (under idealized conditions). In this work we use simulated CO observations which are unbiased and have uncorrelated errors.

The experiments in this work are run from 27 December 2014 18:00:00 UTC to 28 February 2015 00:00:00 UTC. At cold start 65 perturbations of meteorological variables are drawn from the same climatological (static) covariance matrix that was used to generate additive model error. These 65 perturbations are added to the meteorological base state valid at 27 December 2014 18:00:00 UTC. This produces 65 ensemble members for the meteorological variables. Out of the 65 ensemble members the 65th ensemble member is designated as the *truth*. The remaining 64 ensemble members are used for the EnKF estimation experiment. With this approach, the truth member is a plausible member of the ensemble having been generated from the same probability density function. The meteorological observations are drawn from the trajectory of the *truth* at 00, 06, 12 and 18Z every day at which time DA is carried out. The observation networks used in this work are described in section 3.2. An important facet of this work is accounting for surface flux error in the CO estimate. This is accomplished through the use of an ensemble of surface fluxes.

3.1 Surface flux perturbation

The error in surface flux is an important source of error in the CO estimate. This is especially true close to the surface. For example, biases in CO analyses near the surface in polluted urban areas were attributed to surface emissions errors (Inness et al., 2013). Here surface flux error is simulated using perturbed surface flux fields. The posterior of the 4D-Var based GEOS-

Chem inversion constrained by MOPITT observations is used in this work as the *truth*. These posterior surface flux fields are constant over a period of one month (see Figure 2).

255 The surface flux ensemble, of size 64, is generated by using a spectral algorithm (See Appendix A of Mitchell and Houtekamer (2000)). The surface flux perturbations are generated such that they are spatially correlated over a distance (half width) of 1000 km. The standard deviation of the spread is set to 40% of the value of the true surface flux as in Barré et al. (2015). The true surface flux field is used by the 65th ensemble member which generates the truth trajectory. Two sets of 64 surface flux ensemble members are generated, one for January and February 2015, respectively. Each member of the surface flux ensemble
260 is used with a distinct member of the meteorology ensemble.

3.2 Observation networks

The families of meteorological observations used in this work are summarized in Table 1. The location and times of these observations are *real* though the observation values are *simulated*. These meteorological observations are assimilated in all the experiments presented in this work.

Type	0000 UTC	0006 UTC	0012 UTC	0018 UTC
Upper air	54765	3471	51508	2057
Aircraft	78780	54065	56708	78829
Satellite winds	29749	32813	33597	31719
Surface	9927	10314	10271	9984
Scatterometer	18221	17484	19462	16782
GPS-RO	7064	5564	6390	6527

Table 1. Columns shows the typical number of meteorological observations assimilated in each 6 h DA cycle.

The EnKF is tested with five different CO observational networks. These are summarized in Table 2. The first network,

Network	Spatial coverage	Temporal coverage
HYPNET	every 1000 km at levels near 1,5,9 km	every 6 hours
ECCC surface	17 stations (Canada only)	hourly
GAW surface	44 stations	hourly
NOAA surface	69 stations	$\sim$ weekly
MOPITT	1 retrieval per 100 km	Global coverage every 3 days.

Table 2. CO observation networks used in this work.

HYPNET is a hypothetical network. It has spatially dense coverage of in situ observations. In this network the observations are located every 1000 km on three planes : 1 km, 5 km and 9 km. These heights are with respect to the local topography. The globally averaged topography is 376 m. Therefore, the heights of these planes with respect to mean sea level are roughly 1.376 km, 5.376 km and 9.376 km. The locations of observations are shown in Figure 3a.

270   The ECCC surface network (Worthy et al., 2005) consists of 17 observing stations in Canada (see Figure 3c, 3d and Table A1). These stations provide measurements at an hourly frequency. Although the ECCC network has expanded rapidly in the past decade to 25 sites in 2020, only the 17 sites providing hourly measurements in 2015 are simulated here. GAW is an acronym of Global Atmospheric Watch (https://gaw.kishou.go.jp). The 44 stations from the GAW network used in the current work are shown in Figure 3c and listed in Table A2. These stations observe at an hourly frequency. The NOAA surface observation net-
275   work consists of 69 flasks (see Figure 3b). The observations from these flasks are temporally sparse, averaging approximately one per week.

MOPITT (Measurement of pollution in the Troposphere) (Drummond, 1992) is an instrument onboard NASA's Earth Observation Satellite (EOS) Terra that was launched in December 1999. MOPITT is an important component of the global CO observing system because it measures spectra both in the Near InfraRed (NIR) and Thermal InfraRed (TIR) so that its retrieved
280   profiles are sensitive to CO in the lower troposphere during daytime over land, where the flux signal from surface emissions is most readily detected. As a result of this sensitivity to lower tropospheric CO, and the long observational record, MOPITT data are widely used for inverse modelling of CO emissions and for air quality studies (Arellano and Hess, 2006; Fortems-Cheiney et al., 2011; Barré et al., 2015; Jiang et al., 2015a; Yin et al., 2015; Mizzi et al., 2016; Inness et al., 2019; Gaubert et al., 2020; Miyazaki et al., 2020). It has a nadir footprint of 22×22 km and a 612 km cross-track scanning swath, with an orbit that repeats
285   every 3 days. We used V7J MOPITT data with locations thinned to one observation per grid box. The coverage on a particular day is shown in Figure 4. The retrieved profiles are reported on a on 10-layer vertical grid namely, surface, 900 hPa, 800 hPa, ... 100 hPa. The MOPITT retrievals $\mathbf{y}^{obs}$ can be described as follows.

$$\mathbf{y}^{obs} \quad = \quad \mathbf{y}^{pr} + \mathbf{A}(\mathbf{x}^{truth} - \mathbf{y}^{pr}) \tag{7}$$

where $\mathbf{x}^{truth}$ is the true atmospheric profile, $\mathbf{A}$ is the MOPITT averaging kernel, which reflects the sensitivity of the retrieval
290   to the true state and $\mathbf{y}^{pr}$ is the a priori profile used in the retrieval. To generate the pseudo MOPITT data we sample the 65th ensemble model at the locations and times of real MOPITT data, interpolate the profiles to the MOPITT grid, and then apply Eq. 7, with $\mathbf{x}^{truth}$ given by the CO profile from the 65th ensemble member. As a result of the smoothing influence of the retrieval on $\mathbf{x}^{truth}$, the observations operator for MOPITT must also account for this influence. Consequently, the observation operator is analogous to Eq. 7 and is given by,

295    $$\mathbf{Hx} \quad = \quad \mathbf{y}^{pr} + \mathbf{A}(\mathbf{x}^{gem} - \mathbf{y}^{pr}) \tag{8}$$

$\mathbf{x}^{gem}$ is the model profile interpolated to the MOPITT vertical grid.

In the HYPNET, GAW, ECCC and NOAA networks the observation operator is an interpolation operator. The HYPNET, GAW, ECCC and NOAA network are temporally static whereas the MOPITT-like observations change locations depending on the particular DA cycle. The observation errors are set to 10% of the observation values for all networks in our work. The validation of the MOPITT V7J data by Deeter et al. (2017) found that the standard deviation of the retrieved profiles, relative to independent in situ data varied between 10-16 %. As a result, for the synthetic data generated here, we chose a uniform 10% observation error.

In summary, five different observation networks are simulated out of which four have a significant impact on the CO estimation error. The idealistic aspects of the design include the use of simulated (unbiased) observations and ensuring that the truth is consistent with the prior distribution. With these simplifications, and with a uniformly dense observation network such as HYPNET, we can check that our code is correctly implemented. The estimation errors obtained are under best-case scenario and therefore it is expected that higher magnitudes of errors will be obtained with real observations. The benefit of testing EC-CAS with more realistic networks like ECCC, GAW and MOPITT provides a qualitative sense of whether the system is behaving properly since one can expect how networks with data gaps may behave relative to the uniformly dense network. It should be noted that although the observations are simulated here, we are not performing Observing System Simulation Experiments (OSSEs) (See wmo.int/pages/prog/arep/wwrp/new/documents/Final_WWRP_2018_8.pdf for a discussion of designing OSSEs). OSSEs (Prive et al., 2018) are used to compare the results obtained with different observing systems and require careful configuration and tuning of assimilation system parameters so that conclusions might be quantitatively reasonable.

4 Results

This section discusses the improvement in the CO state due to the assimilation of HYPNET, surface observations and MOPITT-like retrievals, in four seperate experiments. The four CO data assimilation experiments are denoted by *EXP_HYP*, *EXP_GAW*, *EXP_NOAA* and *EXP_MOP*. The *EXP_GAW* experiment assimilates the GAW and ECCC surface observations while the *EXP_NOAA* experiment assimilates the NOAA and ECCC surface observations. This improvement is defined with respect to a control experiment which is referred to as *EXP_CNTRL*. The control experiment (*EXP_CNTRL*) assimilates simulated meteorological observations (see Table 1) but does not assimilate simulated CO observations. The CO data assimilation experiments assimilate the same meteorological observations as assimilated by the *EXP_CNTRL* experiment in addition to their CO observations. The results of the *EXP_CNTRL* experiment are discussed in section 4.1. Section 4.2 illustrates the role of dynamically changing spatial correlations in an EnKF update. The results of the four CO data assimilation experiments are described in section 4.3.

4.1 Control experiment

Before delving into results of the CO data assimilation it is important to examine the results of assimilating the meteorological variables. CO is advected by the winds and hence it is critical to ensure that assimilation of meterological observations is working well. Figure 5(a) shows the timeseries of global mean temperature forecast and analysis root mean square error (RMSE) from 27 December 2014 18:00:00 UTC to 28 February 2015 00:00:00 UTC from the *EXP_CNTRL* experiment. See section 2 of the supplemental material for mathematical details of the global mean computation. The RMSE is calculated based on the error between the ensemble mean and the truth which is available at every grid point. As observations are assimilated, the RMSE decreases and stabilizes to $0.5°C$ in about 7 days. The RMSE of forecasts and analyses of horizontal wind components and moisture stabilize at similar rates to that of temperature (figure 5).

The column mean of the ensemble mean of CO averaged over the 7 week assimilation period is shown in Figure 6a. The values of CO are clearly higher in regions of high surface flux (see Figure 2). The CO from central Africa is advected to equatorial Atlantic by the easterly winds. Figure 6b shows the ensemble spread of the CO analysis which is estimated by the standard deviation about the analysis mean. This quantifies the EnKF expected error in the CO mean. The spread in the CO ensemble at any grid point is due to perturbations in the surface flux and spread in the winds. Figure 6c shows the CO analysis RMSE which quantifies the actual error between the ensemble mean and truth. Clearly, comparing Figure 6a and 6c the RMSE is higher in regions of higher values of CO. As noted earlier, the regions with high CO correspond to regions of large surface flux. The similarity of the spatial pattern of CO ensemble spread (Figure 6b) and the RMSE (Figure 6c) and its comparable strength is encouraging because it indicates that the DA system is simulating the actual error well with 64 ensemble members.

The forecast and analysis RMSE are identical because CO observations are not assimilated in the *EXP_CNTRL* experiment. The time series of RMSE over the analysis period is shown by the blue curve in Figure 7a. The RMSE in January 2015 stabilizes to about 19 ppb. The surface flux field changes in February 2015 and hence the RMSE enters a different regime starting on $\sim$ 1 February 2015. The RMSE of the control experiment is a baseline against which the RMSEs from CO data assimilations are compared.

4.2 Role of estimated correlations

The correlations estimated using the forecast ensemble plays a key role in spreading the information from a given CO observation to other grid points for any observational network. The correlation estimate changes dynamically depending on the surface flux perturbations and winds. This state dependence of sample correlation is an important characteristic of ensemble-based filters. The role of the sample correlation and physical localization is illustrated for an observation located at Toronto.

Figure 8 shows the spatial correlation structure for the Toronto location at two different times from *EXP_CNTRL*. In Eq. (1) the term $(\mathbf{y}^o(t) - \mathbf{H}(t)\mathbf{x}^f(t))$ is the *innovation*. This quantity is in observational space and is thus a scalar for the case of a single

observation located at Toronto. The sample correlation $\mathbf{P}^f(t)\mathbf{H}^T(t)$ is used to map the innovation into model space. This is the correlation between the ensemble of $\mathbf{x}^f(t)$ and $\mathbf{H}(t)\mathbf{x}^f(t)$. For simplicity, we take the nearest grid point to Toronto as its actual location so that $\mathbf{H}(t)$ is a row vector of zeros with 1 at the index corresponding ot the Toronto grid point. The innovation in CO at the Toronto grid point updates the CO at all the other grid points in proportion to the correlation as estimated by the forecast ensemble. The regions of high correlation change significantly from 15 January 2015 06:00:00 UTC to 22 January 2015 12:00:00 UTC. Consequently, the impact of the CO observation at Toronto on other grid points is different on 15 January 2015 06:00:00 UTC and 22 January 2015 12:00:00 UTC. In theory (that is, given an infinite ensemble size) a given CO observation should update the CO estimate at all other grid points globally. However, with a small ensemble size, spurious correlations develop and hence physical localization is required so that a given CO observation updates the CO state only within a limited region defined by the horizontal (hlr) and vertical localization radius (vlr) (See section 2.4). The red circle in Figure 8 has radius of $hlr = 2000$ km. The Gaspari-Cohn function (Houtekamer and Mitchell, 1998) (not shown in the Figure) used for physical localization has its maximum at Toronto and decays moving away from the observation's location. This function is used as a weight to modulate the correlation values. As a result, the impact of the observation decays with distance from the observation. Distance-dependent localization assumes that the sample correlation given by the ensemble is less trustworthy (that is more likely to be spurious) as one moves further away from the observation. As noted in section 2.4 variable localization ensures that CO observations do not update meteorological variables. Therefore, the estimates of meteorological variables are the same in all the experiments.

4.3 CO DA experiments

The *EXP_HYP* experiment assimilates HYPNET observations (see section 3.2) in addition to the same meteorological observations assimilated in the *EXP_CNTRL* experiment. The HYPNET observations are assimilated starting on 10 January 2015 18:00:00 UTC after a spin up from 27 December 2014 18:00:00 UTC to 10 January 2015 18:00:00 UTC. This spin up period allows time for the meteorological assimilation to stabilize (Figure 5) before the CO data assimilation begins. This spin up also helps the development of correlations within the CO field.

Figure 6d shows the column averaged CO RMSE for the *EXP_HYP* experiment. Compared to the RMSE for the *EXP_CNTRL* experiment the RMSE decreases substantially because HYPNET observations effectively constrain the CO state. The time series of RMSE for the *EXP_HYP* experiment is shown by the red curve in Figure 7a. The blue and red curves overlap from 27 December 2014 18:00:00 UTC to 10 January 2015 18:00:00 UTC during the spin up period. As soon as CO observations are assimilated starting on 10 January 2015 18:00:00 UTC, the RMSE decreases. The reduction in RMSE due to assimilation of HYPNET observations is ~ 7 ppb. This reduction is defined as the *benefit*,

$$benefit \quad = \quad RMSE(control) - RMSE(DA) \tag{9}$$

385 The *relative benefit* is defined as,

$$relative\_benefit \quad = \quad 100 \times \frac{benefit}{RMSE(control)} \tag{10}$$

The second term in Eq. (9) is the RMSE of the experiment which assimilates CO observations. Since the *EXP_CNTRL* experiment does not assimilate CO observations, *benefit* measures the value of assimilating CO observations from a particular network. This metric quantifies the extent to which CO observations constrain the CO state. Figure 9a shows the spatial struc-

390 ture of *benefit* in the *EXP_HYP* experiment. This figure is basically the difference between Figures 6c and 6d. The *benefit* is positive in most parts of the globe except in parts of Tibet and eastern China. A negative value of *benefit* means that assimilation of CO observations increased the RMSE compared to the *EXP_CNTRL* experiment. Negative values can occur because of the statistical nature of data assimilation. However, if the data assimilation system is well tuned, such regions of negative *benefits* should be few and small, as seen here. By comparing the spatial structure of RMSE in Figure 6c and *benefit* in Figure 9a it is

395 clear that the *benefit* is proportional to the RMSE. This makes sense because where the RMSE is large, the observations have a larger scope for improving the CO state estimate. The mean relative *benefit* (Eq. (10)) in this experiment is 41%. This means that the assimilation of HYPNET observations decreases the control RMSE by 41%.

The time series of RMSE from the *EXP_MOP* experiment is shown by the red curve in Figure 7b. The similarity of the amplitudes (about 9 ppb) of the red curves in Figures 7a and 7b indicates, surprisingly, that the global *benefit* of MOPITT-like

400 data is only a little worse than that due to the hypotetically dense in situ network (HYPNET). However, in our experiments, the observations are unbiased and the observation operator is perfect. The spatial structure of the *benefit* due to the assimilation of MOPITT-like retrievals (*EXP_MOP*) is shown in Figure 9b. By comparing Figure 9a and Figure 9b, it is evident that the *benefit* due to the assimilation of HYPNET observations and MOPITT-like retrievals is also comparable in the column mean, in spite of the different spatio-temporal distribution of observations. The mean relative *benefit* due to the assimilation of MOPITT-like

405 retrievals is 38% while that due to assimilation of HYPNET is 41%.

Figure 10a shows the *benefit* of the *EXP_GAW* experiment. Both the GAW and ECCC networks are assimilated in this experiment. The combined network is temporally dense with observations every hour but is spatially sparse except in Canada and western Europe (Figure 3c and 3d). The relative *benefit* in this experiment is 8%. Figure 10b shows the *benefit* over North America averaged from 0-5 km. All the ECCC stations are located in the bottom 1 km. Figure 10d shows the *benefit* over

410 North America averaged from 0-1 km. The bulk of the *benefit* is in the eastern part of this domain though the ECCC stations are located both in eastern and western Canada. The area of highest *benefit* of about 10-40 ppb is centered on ECCC stations located in Ontario. Even though no stations are located in the USA in this experiment, the *benefit* of observations in Ontario reaches as far as Florida spreading throughout eastern USA. This is because of the flow-dependent spatial correlation between locations of observations in Ontario and the eastern part of USA which is evident in Figure 8, as well as subsequent down-

415 stream transport during the forecast step. The western part of Canada has a weak *benefit* inspite of having several observation

sites in this region. This is because the RMSE in the western region is substantially lower than that in the eastern region (see Figure 10c). Thus there is little scope for the observations to improve upon the control RMSE. The relative *benefit* over North America is 38%.

Figure 10a shows that the assimilation of GAW observations results in significant *benefit* over Europe and parts of central Africa. The *benefit* in Europe is due to high spatial density of GAW stations there. However, with only 5 stations in Africa, a *benefit* of 5-20 ppb in central Africa is produced. Some *benefit* is also seen over north eastern China and Malaysia due to GAW stations located in these regions.

The last experiment, *EXP_NOAA*, assimilates data from the NOAA flask stations in addition to those from the ECCC surface stations. It is seen (figure not shown) that *benefit* over Canada is the same as that seen in *EXP_GAW*. However, globally the NOAA flask stations do not result in any significant *benefit* over any other region. This is because the flask observations are available, on average, only once a week. This experiment is not discussed further in this work.

In the case of the assimilation of HYPNET and MOPITT-like observations (Figures 9a and 9b), many parts of the Atlantic, Pacific, Indian and other oceans show significant *benefit*. The CO surface flux over oceans is practically zero compared to that on land. The HYPNET and MOPITT-like observations over oceans contribute to the *benefit* on oceans. However, the improvement of the CO state over land also contributes to be *benefit* over oceans. For example, any improvement in CO state over central Africa improves the state over tropical Atlantic ocean due to the downwind transport.

In the discussion so far, the horizontal and temporal structure of *benefit* was explored. Figure 11 examines the vertical structure of *benefit*. Figure 11a shows the globally averaged profile of the control RMSE and *benefits* from the three CO DA experiments. The average RMSE of the control experiment (*EXP_CNTRL*) peaks close to the surface with a value of 21 ppb. The average *benefit* in the bottom 4 km is ~ 7 ppb in the *EXP_HYP* and *EXP_MOP* experiments. Comparing the shapes of the blue and red curve to the black curve, the *benefit* is proportional to the control RMSE except in the bottom ~ 1 km. The shape of the *benefit* profile is dictated both by the shape of the control RMSE and the location of observations in the particular network. The *EXP_HYP* profile shows a local peak at 1 km. This is because HYPNET observations are located at 1 km. HYPNET observations are also located at 5 km. However the control RMSE decreases by a factor of 2 from 1 km to 5 km. Consequently the *benefit* also decreases. The peak in the blue profile at ~ 3 km is due to a combination of RMSE values and information content in the MOPITT-like retrievals.

The profiles averaged over Africa (Figure 11b) have similar shapes to those in Figure 11a. This is because both the RMSE and *benefit* in Africa are high compared to other parts of the globe (see Figures 6c and 9). Hence the global average is dominated by values over Africa. The average height of the GAW observations is 2.2 km. The *benefit* in the *EXP_GAW* experiment has a peak value of ~ 4 ppb at 3.5 km. This is because the GAW station located at Mount Kenya (0.06° S,37.29° E) has an altitude of 3678 meters. Additionally the site at Assekrem, Algeria located at 23.26° N,5.63° E is situated at an altitude of 2715 meters.

The EnKF spreads the information content from these observations to the surrounding regions through the flow-dependent covariances used in the analysis step and through downstream transport in the forecast step.

The profiles for North America are shown in Figure 11c. The average height of the ECCC observations is 0.38 km. The *benefit* due to the ECCC observations close to the surface is ~ 4.1 ppb. The *benefit* due to the assimilation of ECCC observations decreases monotonically with height because the RMSE decreases monotonically and also because the ECCC observations cannot constrain the CO state beyond the vertical localization radius. The average height of stations in eastern Canada is 0.212 km. These stations make a major contribution to the *benefit* over North America. Temporally HYPNET observes every 6 hours while ECCC stations observe every hour. Both, the higher temporal frequency and the lower altitude contribute to the higher *benefit* close to the surface in case of the ECCC observations compared to HYPNET observations, which are located at about 1 km.

Figure 11d shows the profiles for Europe. The average height of the GAW observations is 1.13 km. In the case of the GAW network, the *benefit* is 5.9 ppb close to the surface. As in the case of North America the better performance of GAW stations in the bottom 500 meters is a due to both the lower altitude of the stations and higher temporal frequency of observations compared to the HYPNET.

It is evident that the spatio-temporal structure of *benefit* is similar between HYPNET and MOPITT, both horizontally and vertically. This suggests that, in the idealistic setting of unbiased observations and precisely known observation and model error covariances, the performance of MOPITT-like retrievals is similar to insitu observations. It is should be noted that MOPITT-like observations are spatially more dense than our HYPNET observation network. HYPNET has information at three vertical levels while MOPITT has an information content with one or two degrees of freedom (Deeter et al., 2012) so that limited vertical information is provided by the two networks.

5   Conclusions and further work

A new atmospheric composition data assimilation system based on an operational weather forecast model (EC-CAS v1.0) was developed and validated for the estimation of the 3-dimensional state of CO using simulated observations from HYPNET, ECCC, GAW and MOPITT networks. The spread in CO is obtained by perturbing the winds, surface flux fields and physics parametrizations. The CO spread approximately matches the RMSE suggesting that an ensemble size of 64 is acceptable for CO estimation. However, these conclusions are based on the assimilation of simulated observations which are unbiased.

These experiments lead to a qualitative understanding of the decrease in RMSE due to the assimilation of observed CO from realistic networks. With all of the networks it is seen that the benefit due to the assimilation of CO observations is proportional to the CO RMSE. Another factor, which controls the pattern of the benefit, is the locations of observations. For example, the GAW network has only one station in central Africa. The observations from this station are able to effectively constrain the

CO state within 2000 km, which is the localization radius used in these experiments. The benefit is the highest in the plane at which this observation is located. The CO state close to the surface is better constrained by observations in the lowermost 500 m than observations at 1 km. This is suggested by the results in North America and Europe. The CO state over the ocean is

480   constrained due to the improvement of the CO state over surface flux-rich land regions which is transported downstream during the forecast and also due to the assimilation of observations over the oceans. In the case of MOPITT-like data assimilation, the benefit in central Africa (which is the region with the strongest surface flux) ranges from 10 to over 40 ppb. The downwind transport results in a benefit of 5 to 40 ppb over the tropical Atlantic. The benefits over south and east Asia range from 2 to 20 ppb. These quantitative findings are expected to change when real observations are assimilated. Biases in observations

485   and correlations in the observational errors along with unaccounted model errors make assimilation of real observations more challenging so that the error reductions are expected to be smaller.

This work has presented only the very first step in the development of EC-CAS. There are many further stages of development because the goal of EC-CAS is to estimate the 3-dimensional fields of CO, CO_2 and CH_4 and their surface fluxes along with meteorological fields by assimilating all available observations of meteorological variables and chemical species using

490   an ensemble smoother. These include both in situ and remotely sensed measurements. The immediate next step is to modify EC-CAS 1.0 to allow the update of the CO surface flux by CO observations since we demonstrated here that the CO state estimation is working well. After the ability to estimate surface fluxes is demonstrated EC-CAS will be tested for estimation of CO and CO_2 3-dimensional fields and their surface fluxes using real observations. The estimates of surface flux can be improved by using a smoother (Liebelt, 1967) rather than a filter since a smoother assimilates observations earlier as well as

495   later than the analysis time. Ultimately, an ensemble Kalman smoother (Bocquet, 2016) will be developed.
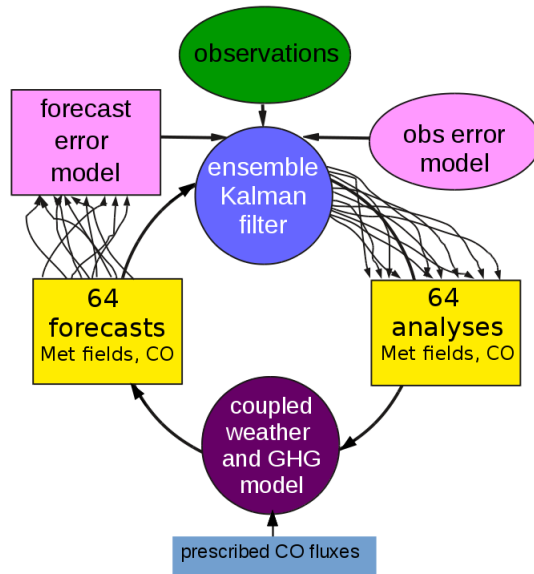
Figure 1. EC-CAS v1.0. There is an ensemble of 64 prescribed CO surface fluxes. In EC-CAS v1.0 surface flux fields are not estimated. Instead, the perturbed flux field is used to account for uncertainty in CO due to error in the surface flux. The 64-member forecast ensemble is used along with the observations and the statistics of observation errors as inputs to the EnKF. The 64 analyses of meteorology and CO generated by the EnKF are used as initial conditions for the next 6 hour forecast. This cycle repeats every 6 h.
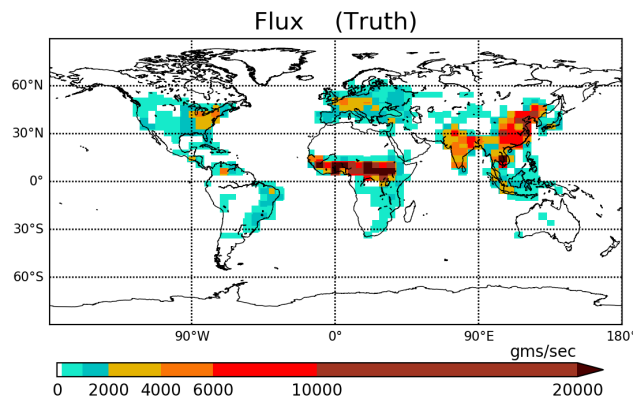
Figure 2. The true CO surface flux field for January 2015.
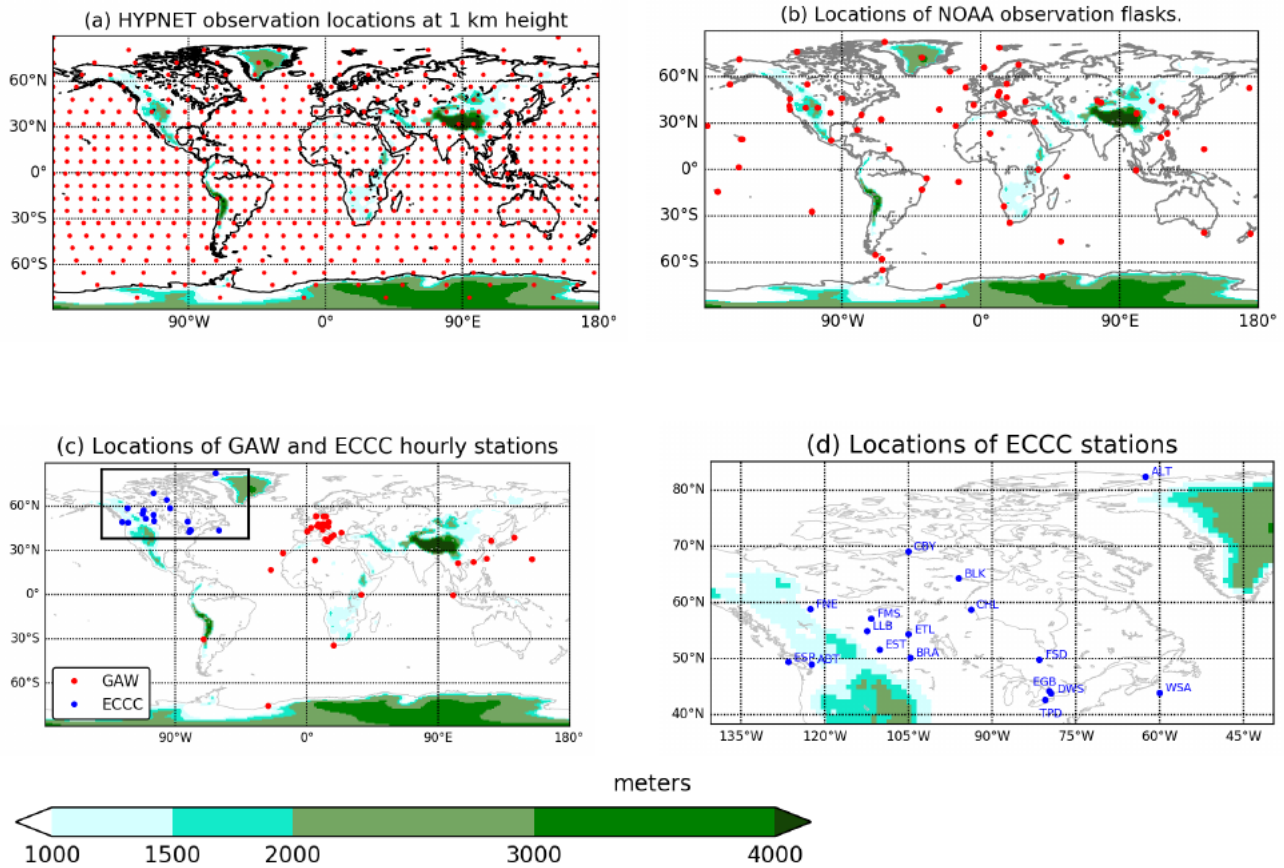
Figure 3. In each panel, topography is shown by the color. (a) HYPNET exists at 1 km, 5 km and 9 km. At each of these levels the observations are located 1000 km apart in the horizontal. There are 622 observations locations at each height and total of $622 \times 3 = 1866$ observations every 6 hours. (b) The locations of flask observations from the NOAA network. (c) The GAW and ECCC station locations. (d) The ECCC station locations also shown in panel (c).
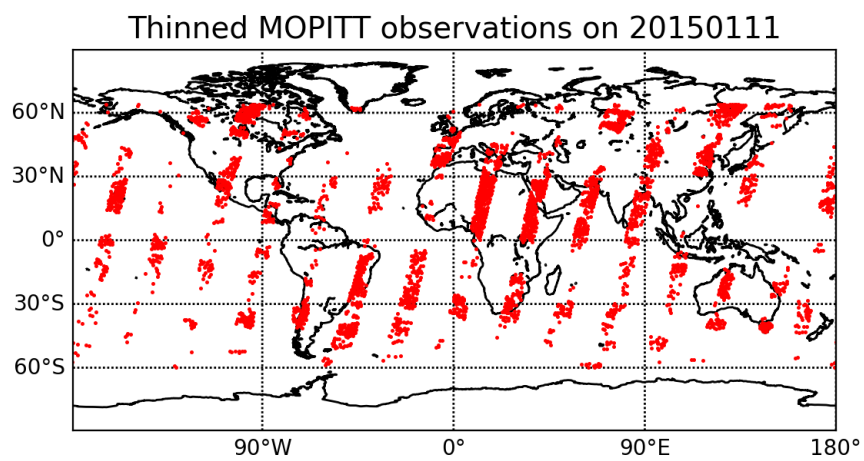
Figure 4. An example of the distribution of MOPITT satellite observations. Thinned MOPITT orbits on 11 January 2015 00:00:00 UTC are shown.
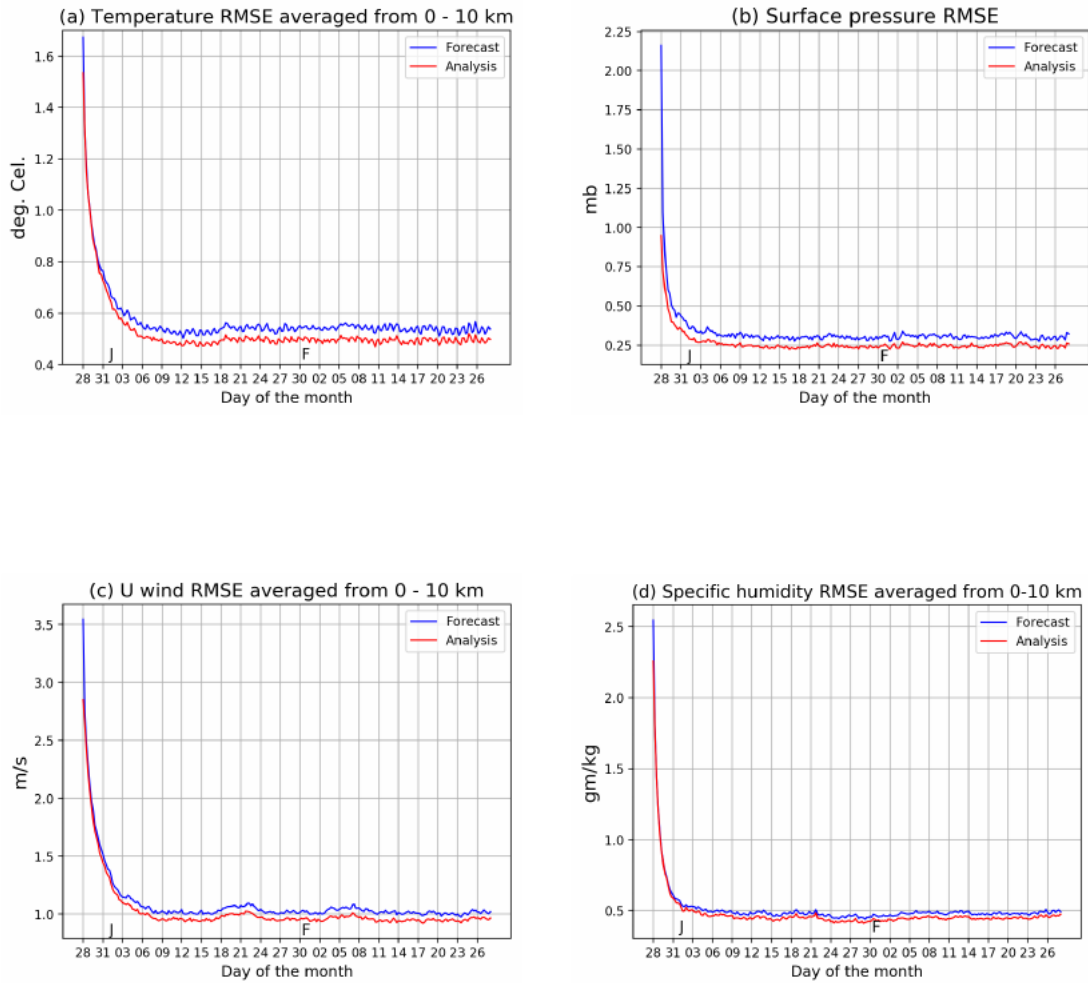
Figure 5. The timeseries of RMSE of meteorological variables from the *EXP_CNTRL* are shown. J and F marked on the xaxis indicate the start of January and February respectively. The analyses is shown in red color and the forecast RMSE in blue.
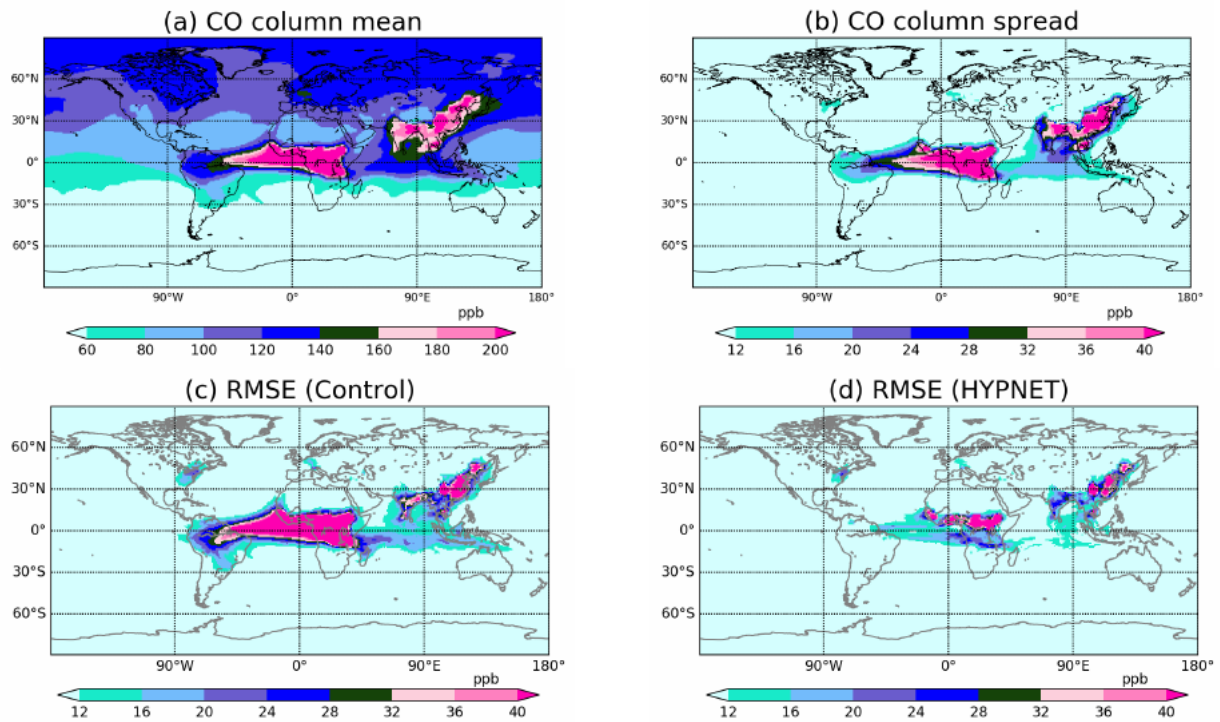
Figure 6. In each panel, column means (0-5 km) averaged from 10 January 2015 18:00:00 UTC to 28 February 2015 00:00:00 UTC are shown. (a) CO ensemble mean of the control experiment. (b) CO ensemble spread of the control experiment. (c) RMSE of the control experiment. (d) RMSE of the *EXP_HYP* experiment.
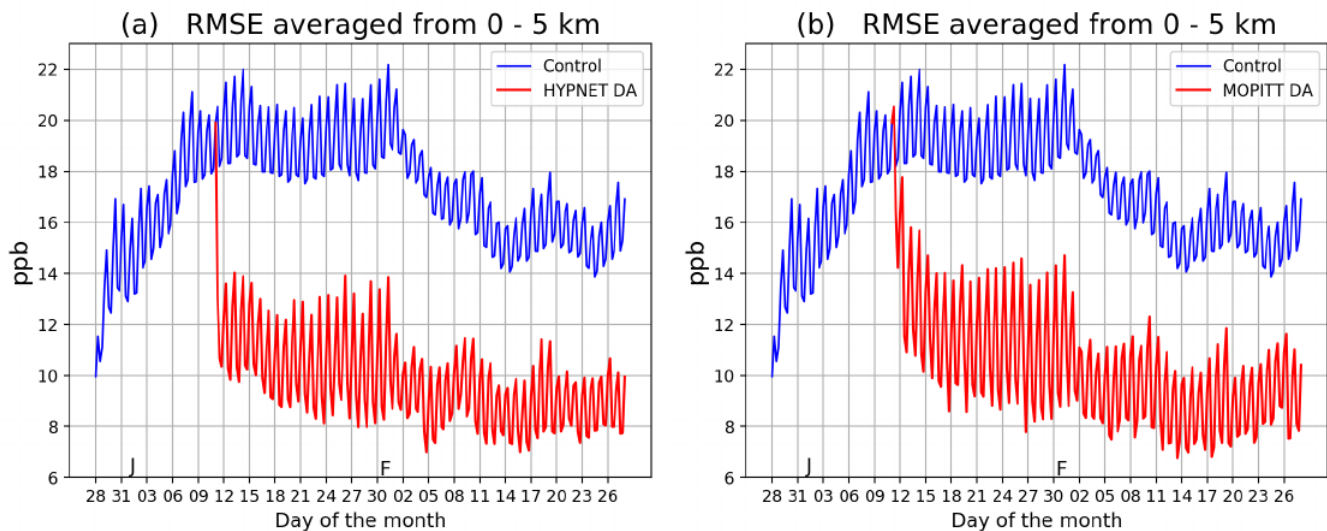
Figure 7. Column (0-5 km) mean RMSE of CO analyses from various experiments : (a) The control, *EXP_CNTRL* (blue curve) and the DA experiment assimilating HYPNET observations, *EXP_HYP* (red curve). (b) The control, *EXP_CNTRL* (blue curve) and the DA experiment assimilating MOPITT-like observations, *EXP_MOP* (red curve). The blue curves in panel (a) and (b) are identical. J and F marked on the xaxis indicate the start of January and February respectively. The 24 h oscillations in the curves are meteorology induced.
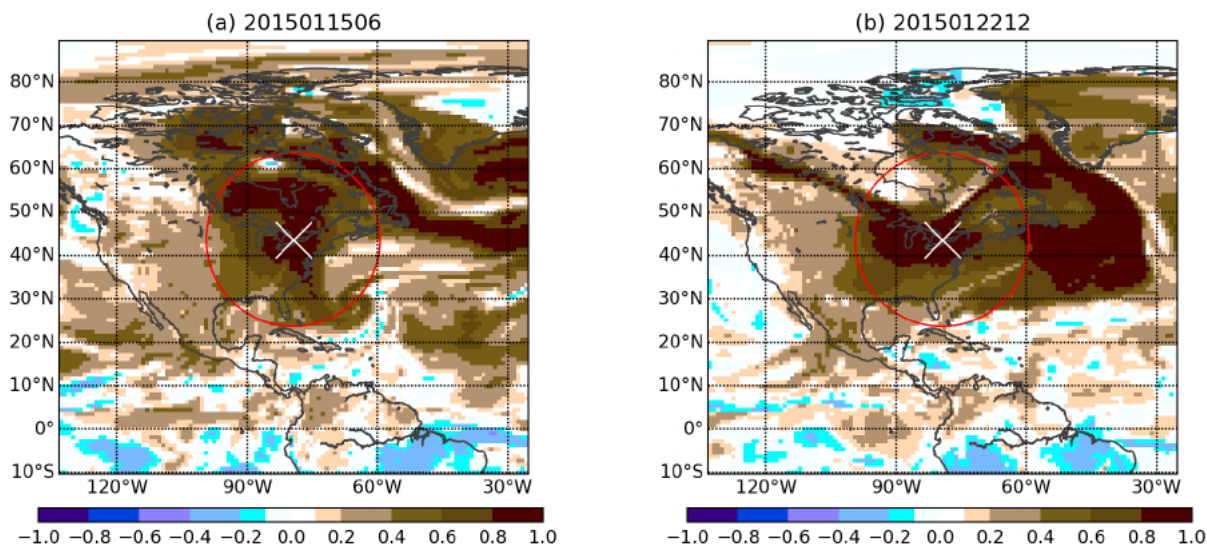
Figure 8. The spatial correlation of CO between Toronto (shown by the white cross) and other locations in the horizontal plane defined by the lowest model level. The red circle of radius 2000 km shows the horizontal localization. The correlation is estimated by using the 64 forecast ensemble members.
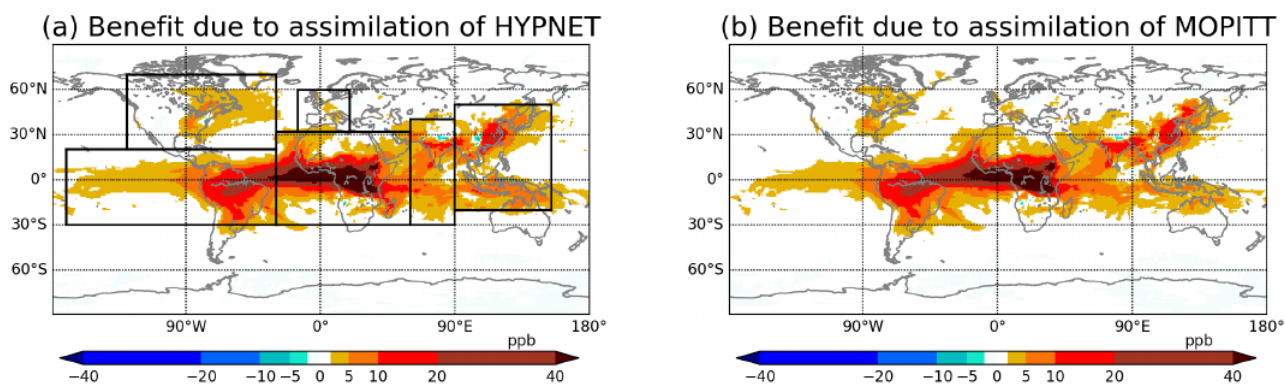
Figure 9. Column (0-5 km) mean benefit averaged from 10 January 2015 18:00:00 UTC to 28 February 2015 00:00:00 UTC. In panel (a), the marked boxes show the domains of North America, South America, Europe, Africa, South Asia and East Asia. These domains are used in Figure 11. Note that all the domains contain both ocean and land. The South American domain includes a large part of the Pacific ocean.
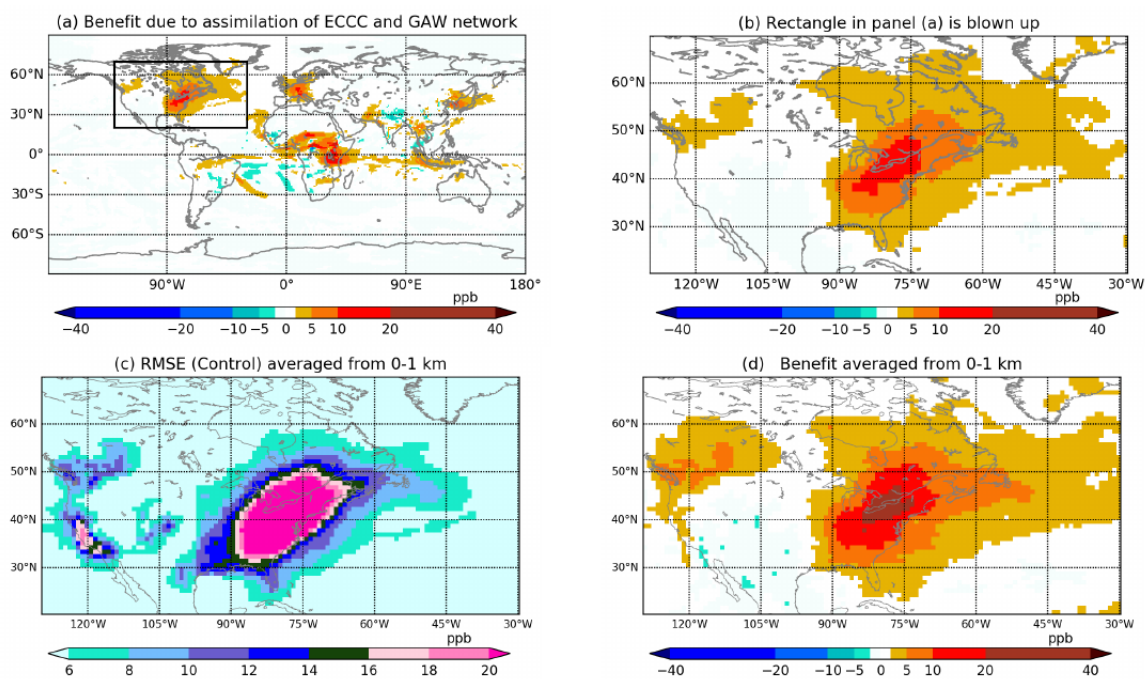
Figure 10. In all panels averages from 10 January 2015 18:00:00 UTC to 28 February 2015 00:00:00 UTC are shown.
(a) Column (0-5 km) mean benefit from *EXP_GAW*. (b) The North American domain from panel (a). (c) Column (0-1 km) mean RMSE from *EXP_CNTRL*. (d) Column (0-1 km) mean benefit from *EXP_GAW*.
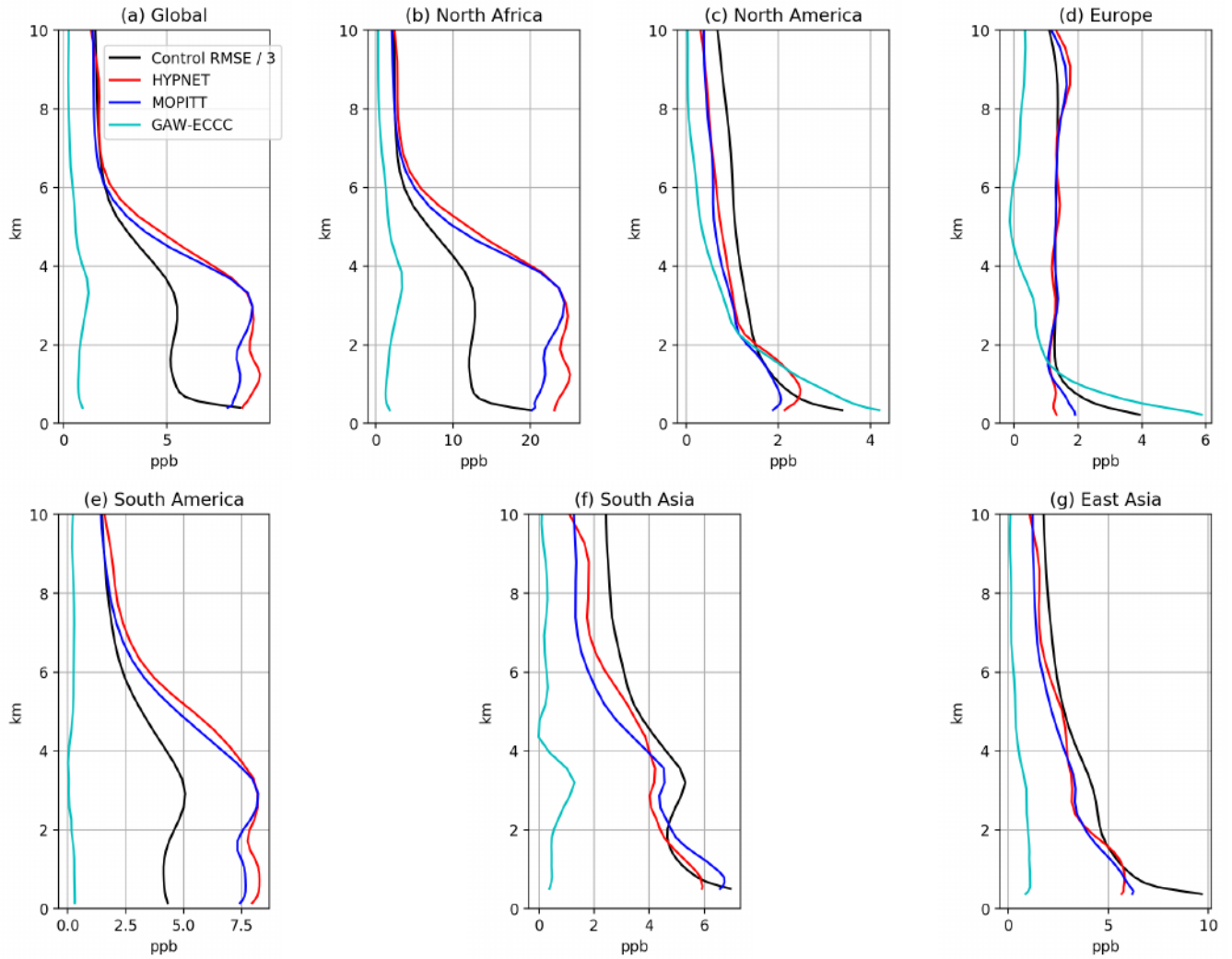
Figure 11. Profiles of benefit and control RMSE averaged over different domains. In each panel the black curve shows the control RMSE scaled down by a factor of 3. The colored curves show the benefits due to the assimilation of three different observational networks (*EXP_HYP*, *EXP_MOP* and *EXP_GAW*). Panel (a) shows the globally averaged profiles. The other panels show profiles averaged over domains shown in figure 9a. The limits on the x-axis are different in each panel.

Appendix

	Code	Station name	Latitude	Longitude	Altitude
1	ABT	Abbotsford	49.01	−122.34	60.3
2	ALT	Alert	82.45	−62.52	200.0
3	BLK	Baker Lake	64.33	−96.01	94.8
4	BRA	Bratts Lake	50.20	−104.71	595.0
5	CBY	Cambridge Bay	69.13	−105.06	35.0
6	CHL	Churchill	58.74	−93.82	29.0
7	DWS	Downsview	43.78	−79.47	198.0
8	EGB	Egbert	44.23	−79.78	251.0
9	ESP	Estevan Point	49.38	−126.54	7.0
10	EST	Esther Alberta	51.67	−110.21	707.0
11	ETL	East Trout Lake	54.35	−104.99	493.0
12	FMS	Fort McKay	57.15	−111.64	250.0
13	FNE	Fort Nelson	58.84	−122.57	361.0
14	FSD	Fraserdale	49.88	−81.57	210.0
15	LLB	Lac LaBiche	54.95	−112.47	540.0
16	TPD	Turkey Point	42.64	−80.55	231.0
17	WSA	Sable Island	43.93	−60.01	5.0

Table A1. Information about ECCC surface sites used in this study. The altitude is in meters above sea level.

	Code	Station name	Latitude	Longitude	Altitude		Code	Station name	Latitude	Longitude	Altitude
1	AMY	Anmyeon-do	36.5383	126.3300	71.0	23	IZO	Izaña	28.3090	−16.4993	2403.0
2	ASK	Assekrem	23.2667	5.6333	2715.0	24	JFJ	Jungfraujoch	46.5475	7.9851	3580.0
3	BEO	Moussala	42.1792	23.5856	2931.0	25	KMW	Kollumerwaard	53.3333	6.2667	3.5
4	BKT	Bukit Kototabang	−0.2019	100.3180	874.0	26	KOS	Kosetice	49.5833	15.0833	535.0
5	CGR	Capo Granitola	37.6667	12.6500	9.0	27	KTB	Kloosterburen	53.4000	6.4200	0.0
6	CMN	Monte Cimone	44.1667	10.6833	2172.0	28	KVV	Krvavec	46.2973	14.5333	1750.0
7	CPT	Cape Point	−34.3534	18.4897	260.0	29	LMT	Lamezia Terme	38.8763	16.2322	14.0
8	CUR	Monte Curcio	39.3160	16.4232	1800.9	30	MKN	Mt. Kenya	−0.0622	37.2972	3682.5
9	CVO	Cape Verde	16.8640	−24.8675	20.0	31	MNM	Minamitorishima	24.2883	153.9833	27.1
10	ECO	Lecce	40.3358	18.1245	86.0	32	NGL	Neuglobsow	53.1428	13.0333	62.0
11	GAT	Gartow	53.0657	11.4429	99.0	33	PAY	Payerne	46.8129	6.9435	494.5
12	GAT	Gartow	53.0657	11.4429	129.0	34	PDI	Pha Din	21.5731	103.5157	1478.0
13	GAT	Gartow	53.0657	11.4429	201.0	35	PDM	Pic du Midi	42.9372	0.1411	2881.0
14	GAT	Gartow	53.0657	11.4429	285.0	36	PUY	Puy de Dome	45.7723	2.9658	1467.0
15	GAT	Gartow	53.0657	11.4429	410.0	37	RIG	Rigi	47.0674	8.4633	1036.0
16	GLH	Giordan	36.0700	14.2200	167.0	38	RYO	Ryori	39.0319	141.8222	280.0
17	HBA	Halley	−75.3500	−26.3900	38.0	39	SNB	Sonnblick	12.9578	47.0542	3111.0
18	HKG	Hok Tsui	22.2095	114.2578	60.0	40	SSL	Schauinsland	47.9000	7.9167	1205.0
19	HPB	Hohenpeissenberg	47.8000	11.0200	1003.0	41	TLL	El Tololo	−30.1683	−70.8036	2159.0
20	HPB	Hohenpeissenberg	47.8011	11.0246	1035.0	42	YON	Yonagunijima	24.4667	123.0106	50.0
21	HPB	Hohenpeissenberg	47.8011	11.0246	1078.0	43	ZSF	Zugspitz	47.4165	10.9796	2670.0
22	HPB	Hohenpeissenberg	47.8011	11.0246	1116.0	44	ZUG	Zugspitz-Gipfel	47.4211	10.9859	2965.5

Table A2. Information about GAW surface sites used in this study. The altitude is in meters above sea level.

Code and data availability. The source code is publicly available at https://doi.org/10.5281/zenodo.3908545 under the GNU Lesser General Public License version 2.1 (LGPL v2.1) or ECCC's Atmospheric Sciences and Technology licence version 3. The model data output are available at http://crd-data-donnees-rdc.ec.gc.ca/CCMR/pub/2020_Khade_ECCAS_all_data/.

500 *Author contributions.* Vikram Khade developed the code related to the extension of EnKF to CO. Vikram Khade and Saroja Polavarapu designed, carried out the experiments and interpreted them. Michael Neish prepared the input data required for the experiments. This includes but is not limited to the regridding of surface flux fields used as the truth. Pieter Houtekamer supervised the development of the code. Seung-Jong Baek helped with code debugging and optimization of the performance of the code. Dylan Jones played an important role in the designing of the experiments and interpretation of the results. Tailong He carried out the 4D-Var inversion using GEOS-Chem to produce
505 surface flux fields used as truth. Sylvie Gravel helped with the development needed to include CO as a species in the forecast model, GEM-MACH-GHG.

Competing interests. The authors declare that they have no conflict of interest.

Acknowledgements. We are grateful to the following people for their advice or assistance. Douglas Chan helped with the understanding of the surface observations. Doug Worthy and his team provided the ECCC surface observations. Feng Deng helped with interpretation of results.
510 Jinwong Kim ran few experiments. Michael Sitwell provided the code to convert CO observations into BURP format. Yves Rochon provided the MOPITT data and also the code for MOPITT forward operator. Jim Drummond helped with the understanding of the MOPITT data. We thank Michael Sitwell and Yves Rochon for helpful comments on a previous version of the manuscript. We thank the two anonymous reviewers for comments which helped to improve this manuscript.

References

515   Abatzoglou, J.T., and Williams, A.P. : Impact of anthropogenic climate change on wildfires across western US forests. Proceedings of the National Academy of Sciences of the United States of America,113(42), 11770-11775,2016.

Anderson,J.L.: An ensemble adjustment Kalman filter for data assimilation. Mon. Wea. Rev., 129, 2884-2903, 2001.

Anselmo, D., M.D. Moran, S. Menard, V. Bouchet, P. Makar, W. Gong, A. Kallaur, P.-A. Beaulieu, H. Landry, C. Stroud, P. Huang, S. Gong, and D. Talbot, 2010.A new Canadian air quality forecast model: GEM-MACH15. Proc. 12th AMS Conf. on Atmos. Chem., Jan. 17-21,
520   Atlanta, GA, American Meteorological Society, Boston, MA, 6 pp. [see http://ams.confex.com/ams/pdfpapers/165388.pdf]

Arellano, A. F. and Hess, P. G. : Sensitivity of top-down estimates of CO sources to GCTM transport, Geophys. Res. Lett., 33, L21807, http://doi:10.1029/2006GL027371, 2006.

Bannister, R.N.: A review of forecast error covariance statistics in atmospheric variational data assimilation. I : characteristics and measurements of forecast error covariances. QJRMS, 134(637),1951-1970,2008.

525   Barré, J., Gaubert B., Arellano A.J., Worden H.M., Edwards, D.P., Deeter M.N., Anderson J.L., Raeder K., Collins N., Tilmes S., Clerbaux C., Emmons L.K., Pfister G., Coheur P-F., Hurtmans D. : Assessing the impacts of assimilating IASI and MOPITT CO retrievals using CESM-CAM-chem and DART,J.Geophy. Res. Atmos., 120. doi:10.1002/2015JD023467, 2015.

Bloom, S., Takacs, L., DaSilva, A., and Ledvina, D.: Data assimilation using incremental analysis updates, Mon. Wea. Rev., 124: 1256-1271, 1996.

530   Bocquet, M.: Localization and the iterative ensemble Kalman smoother, QJRMS, 142, 1075-1089, 2016, DOI : 10.1002/qj.2711

Bruhwiler, L., Dlugokencky, E., Masarie, K., Ishizawa, M., Andrews, A., Miller, J., Sweeney, C., Tans, P., and Worthy, D.: CarbonTracker-CH4: an assimilation system for estimating emissions of atmospheric methane, Atmos. Chem. Phys., 14, 8269-8293, https://doi.org/10.5194/acp-14-8269-2014, 2014.

Cohn, S.E., and Parrish,D.F.: The behavior of forecast error covariances for a Kalman filter in two dimensions. Mon. Wea. Rev., 119, 1757-
535   1785, 1991.

Côté, J., Gravel, S., Methot, A., Patoine, A., Roch, M., and Staniforth, A.: The operational CMC-MRB Global Environmental Multiscale (GEM) model. Part I: Design considerations and formulation, Mon. Wea. Rev., 126, 1373-1395, doi:10.1175/1520-0493(1998)126<1373:TOCMGE>2.0.CO;2., 1998a.

Côté, J., Desmarais, J.-G., Gravel, S., Methot, A., Patoine, A., Roch, M. and Staniforth, A.: The operational CMC-MRB
540   Global Environmental Multiscale (GEM) model. Part II: Results, Mon. Wea. Rev., 126, 1397-1418, doi:10.1175/1520-0493(1998)126<1397:TOCMGE>2.0.CO;2,1998b.

Crowell, S., Baker, D., Schuh, A., Basu, S., Jacobson, A. R., Chevallier, F., Liu, J., Deng, F., Feng, L., McKain, K., Chatterjee, A., Miller, J. B., Stephens, B. B., Eldering, A., Crisp, D., Schimel, D., Nassar, R., O'Dell, C. W., Oda, T., Sweeney, C., Palmer, P. I., and Jones, D. B. A.: The 2015-2016 carbon cycle as seen from OCO-2 and the global in situ network, Atmos. Chem. Phys., 19, 9797-9831,
545   https://doi.org/10.5194/acp-19-9797-2019, 2019.

Deeter, M., Worden, H., Edwards, D., Gille, J., and Andrews, A.: Evaluation of MOPITT retrievals of lower-tropospheric carbon monoxide over the United States, J. Geophys. Res., 117, D13306, doi:10.1029/2012JD017553,2012.

Deeter, M., Edwards, D., Francis, G., Gille, J., Martinez-Alonso, S., Worden, H., and Sweeeney, C.: A climate-scale satellite record for Carbon monoxide : the MOPITT version 7 product, Atmos. Meas. Tech., 10, 2533-2555, https://doi.org/10.5194/amt-10-2533-2017,
550   2017.

Drummond, J.R.: Measurement of Pollution in the Troposhere (MOPITT). The use of EOS for studies of Atmospheric Physics,77-101,1992.

ECCC, Pollutant Inventories and Reporting division : National Inventory Report 1990-2018 : Greenhouse Gas sources and sinks in Canada, 2020, http://publications.gc.ca/collections/collection_2020/eccc/En81-4-2018-3-eng.pdf

Flannigan,M.D., Krawchuk, M.A., de Groot,W.J., and Growman,L.M : Implications of changing climate for global wildland fire, International Journal of Wildfire,18,483-507,2009

Fortems-Cheiney, A., F. Chevallier, I. Pison, P. Bousquet, S. Szopa, M. N. Deeter, and C. Clerbaux : Ten years of CO emissions as seen from Measurements of Pollution in the Troposphere (MOPITT), J. Geophys. Res., 116, D05304, doi:10.1029/2010JD014416, 2011.

Gaspari, G., and Cohn, S.E.: Construction of correlation functions in two and three dimensions. Quart. J. Roy. Meteor. Soc.,125,723-757, 1999.

Gaubert, B., Arellano Jr., A., Barre, J., Worden, H., Emmons, L., Tilmes, S., Buchholz, R., Vitt, F., Raeder, K., Collins, N., Anderson, J., Wiedinmyer, C., Martinez Alonso, S., Edwards, D., Andreae, M., Hannigan, J., Petri, C., Strong, K., and Jones, N.: Toward a chemical reanalysis in a coupled chemistry-climate model : An evaluation of MOPITT CO assimilation and its impact on tropospheric compostion. Quart. J. Geophys. Res. Atmos.,121,7310-7343,2016.

Gaubert, B., Emmons, L. K., Raeder, K., Tilmes, S., Miyazaki, K., Arellano Jr., A. F., Elguindi, N., Granier, C., Tang, W., Barré, J., Worden, H. M., Buchholz, R. R., Edwards, D. P., Franke, P., Anderson, J. L., Saunois, M., Schroeder, J., Woo, J.-H., Simpson, I. J., Blake, D. R., Meinardi, S., Wennberg, P. O., Crounse, J., Teng, A., Kim, M., Dickerson, R. R., He, H., and Ren, X.: Correcting model biases of CO in East Asia: impact on oxidant distributions during KORUS-AQ, Atmos. Chem. Phys. Discuss., https://doi.org/10.5194/acp-2020-599, 2020.

Ghil, M., Cohn, S., Tavantzis, J., Bube, K., and Isaacson, E. : Applications of estimation theory to numerical weather prediction. Dynamic meteorology - data assimilation methods. Eds. Bengtsson,L., Ghil,M., and Kallen, E.,Springer-verlag, Heidelberg, 134-224, 1981.

Girard, C., Plante, A., Desgagne, M., McTaggart-Cowan, R., Cote, J., Charron, M., Gravel, S., Lee, V., Patoine, A., Qaddouri, A., Roch, M., Spacek, L., Tanguay, M., Vaillancourt, P. A., Zadra, A.: Staggered Vertical Discretization of the Canadian Environmental Multiscale (GEM) Model Using a Coordinate of the Log-Hydrostatic-Pressure Type. Mon. Wea. Rev., 142, 113, DOI: 10.1175/MWR-D-13-00255.1, 2014.

Gong, W., P.A. Makar, J. Zhang, J. Milbrandt, S. Gravel, K.L. Hayden, A.M. Macdonald, and W.R. Leaitch, 2015. Modelling aerosol-cloud-meteorology interaction: A case study with a fully coupled air quality model (GEM-MACH).Atmos. Environ., http://dx.doi.org/10.1016/j.atmosenv.2015.05.062, 115, 695-715,2015.

Hamill, T.M., Whitaker, J.S. and Snyder, C.: Distance-dependent filtering of background error covariance estimates in an ensemble Kalman filter. Mon. Wea. Rev., 129, 2776-2790, 2001.

Houtekamer, P.L., Lefaivre, L., Derome, J., Richie, H. and Michell, H.L.: A system simulation approach to ensemble predictions. Mon. Wea. Rev., 124, 1225-1242, 1996.

Houtekamer, P.L., and Mitchell, H.L.: Data assimilation using an Ensemble Kalman Filter technique. Mon. Wea. Rev., 126(3), 796-811, 1998.

Houtekamer, P.L., and Mitchell, H.L.: A sequential ensemble Kalman filter for atmospheric data assimilation. Mon. Wea. Rev., 129, 123-137, 2001.

Houtekamer, P.L., and Mitchell, H.L.: Ensemble Kalman filtering. QJRMS, 131, 3269-3289, 2005.

Houtekamer, P.L., Deng, X., Mitchell, H.L., Baek, S.-J. and Gagnon, N.: Higher Resolution in an Operational Ensemble Kalman Filter, Mon. Wea. Rev., 142, 1143-1162, 2014.

Houtekamer, P.L., and Zhang, F.: Review of the Ensemble Kalman Filter for atmospheric data assimilation. Mon. Wea. Rev., 144(12), 4489-4532, 2016.

Houtekamer, P.L., Buehner, M., and Chevrotiere, M.: Using the hybrid gain algorithm to sample data assimilation uncertainty, QJRMS., 145, 35-56, 2019.

Inness, A., Baier, F., Benedetti, A., Bouarar, I., Chabrillat, S., Clark, H., Clerbaux, C., Coheur, P., Engelen, R. J., Errera, Q., Flemming, J., George, M., Granier, C., Hadji-Lazaro, J., Huijnen, V., Hurtmans, D., Jones, L., Kaiser, J. W., Kapsomenakis, J., Lefever, K., Leitão, J., Razinger, M., Richter, A., Schultz, M. G., Simmons, A. J., Suttie, M., Stein, O., Thépaut, J.-N., Thouret, V., Vrekoussis, M., Zerefos, C., and the MACC team: The MACC reanalysis: an 8 yr data set of atmospheric composition, Atmos. Chem. Phys., 13, 4073-4109, https://doi.org/10.5194/acp-13-4073-2013, 2013.

Inness, A., Blechschmidt, A.-M., Bouarar, I., Chabrillat, S., Crepulja, M., Engelen, R. J., Eskes, H., Flemming, J., Gaudel, A., Hendrick, F., Huijnen, V., Jones, L., Kapsomenakis, J., Katragkou, E., Keppens, A., Langerock, B., de Mazière, M., Melas, D., Parrington, M., Peuch, V. H., Razinger, M., Richter, A., Schultz, M. G., Suttie, M., Thouret, V., Vrekoussis, M., Wagner, A., and Zerefos, C.: Data assimilation of satellite-retrieved ozone, carbon monoxide and nitrogen dioxide with ECMWF's Composition-IFS, Atmos. Chem. Phys., 15, 5275-5303, https://doi.org/10.5194/acp-15-5275-2015 , 2015.

Inness, A., Ades, M., Agustí-Panareda, A., Barré, J., Benedictow, A., Blechschmidt, A.-M., Dominguez, J. J., Engelen, R., Eskes, H., Flemming, J., Huijnen, V., Jones, L., Kipling, Z., Massart, S., Parrington, M., Peuch, V.-H., Razinger, M., Remy, S., Schulz, M., and Suttie, M.: The CAMS reanalysis of atmospheric composition, Atmos. Chem. Phys., 19, 3515-3556, https://doi.org/10.5194/acp-19-3515-2019 , 2019.

Janssens-Maenhout, G., Crippa, M., Guizzardi, D., Dentener, F., Muntean, M., Pouliot, G., Keating, T., Zhang, Q., Kurokawa, J., Wankmüller, R., Denier van der Gon, H., Kuenen, J. J. P., Klimont, Z., Frost, G., Darras, S., Koffi, B., and Li, M.: HTAP_v2.2: a mosaic of regional and global emission grid maps for 2008 and 2010 to study hemispheric transport of air pollution, Atmos. Chem. Phys., 15, 11411-11432, https://doi.org/10.5194/acp-15-11411-2015, 2015.

Jiang, Z., Jones, D. B. A., Kopacz, M., Liu, J., Henze, D. K., and C. Heald : Quantifying the impact of model errors on top-down estimates of carbon monoxide emissions using satellite observations, J. Geophys. Res., 116, D15306, doi:10.1029/2010JD015282, 2011.

Jiang, Z., Jones, D. B. A., Worden,H. M.,Deeter, M. N., Henze,D. K., Worden, J., Bowman, K. W., Brenninkmeijer, C. A. M., and Schuck, T. J. : Impact of model errors in convective transport on CO source estimates inferred from MOPITT CO retrievals, J. Geophys. Res. Atmos., 118, 2073-2083, https://doi:10.1002/jgrd.50216, 2013.

Jiang, Z., Jones, D. B. A., Worden, H. M., and Henze, D. K.: Sensitivity of top-down CO source estimates to the modeled vertical structure in atmospheric CO, Atmos. Chem. Phys., 15, 1521-1537, https://doi.org/10.5194/acp-15-1521-2015 , 2015a.

Jiang, Z., Jones, D. B. A., Worden, J., Worden, H. M., Henze, D. K., and Wang, Y. X.: Regional data assimilation of multi-spectral MOPITT observations of CO over North America, Atmos. Chem. Phys., 15, 6801-6814, https://doi.org/10.5194/acp-15-6801-2015 , 2015b.

Jiang, Z., Worden, J. R., Worden, H., Deeter, M., Jones, D. B. A., Arellano, A. F., and Henze, D. K.: A 15-year record of CO emissions constrained by MOPITT CO observations, Atmos. Chem. Phys., 17, 4565-4583, https://doi.org/10.5194/acp-17-4565-2017, 2017.

JPL: Chemical Kinetics and Photochemical Data for Use in Atmospheric Studies. Evaluation Number 17. NASA Panel for Data Evaluation. June 10, 2011. Available from: https://jpldataeval.jpl.nasa.gov/previous_evaluations.html

Kain, J.S., and Fritsch, J.M.: A one-dimensional entraining/detraining plume model and its application in convective parameterizations, J. Atmos. Sci. 47, 2784-2802, 1990.

Kain, J.S.: The Kain-Fritsch convective parameterization: an update, J. Appl. Meteorol. 43, 170-181, 2004.

Kang, J.-S., Kalnay, E., Liu, J., Fung, I., Miyoshi, T. and Ide ,K.: "Variable localization" in an ensemble Kalman filter: Application to the carbon cycle data assimilation, J. Geophys. Res., 116, D09110, doi:10.1029/2010JD014673, 2011.

Kim, J., Polavarapu, S., Chan, D., and Neish, M.: The Canadian atmospheric transport model for simulating greenhouse gas evolution on regional scales: GEM-MACH-GHG v.137-reg, Geosci. Model Dev. Discuss., https://doi.org/10.5194/gmd-2019-123, 2020.

Khade, V., Neish, M., Houtekamer, P.L., Polavarapu, S., Baek, S-J., and Jones. D.B.A. (2020, June 29). EC-CAS v1.0. Zenodo. https://doi.org/10.5281/zenodo.3908545

Kopacz, M., Jacob, D. J., Fisher, J. A., Logan, J. A., Zhang, L., Megretskaia, I. A., Yantosca, R. M., Singh, K., Henze, D. K., Burrows, J. P., Buchwitz, M., Khlystova, I., McMillan, W. W., Gille, J. C., Edwards, D. P., Eldering, A., Thouret, V., and Nedelec, P.: Global estimates of CO sources with high resolution by adjoint inversion of multiple satellite datasets (MOPITT, AIRS, SCIAMACHY, TES), Atmos. Chem. Phys., 10, 855-876, https://doi.org/10.5194/acp-10-855-2010, 2010.

Lawson, W.G., and Hansen, J.A.: Implications of stochastic and deterministic filter as ensemble-based data assimilation methods in varying regimes of error growth. Mon. Weather. Rev., 132, 1966-1981, 2004.

Liebelt, P.B : An introduction to optimal estimation, Addison-Wesley publishing company, Reading, USA, 1967.

Mitchell, H.L. and Houtekamer, P.L.: An adaptive ensemble Kalman filter. Mon. Wea. Rev., 128, 416-433, 2000.

Miyazaki,K., Maki T., Patra P. and Nakazawa, T. : Assessing the impact of satellite, aircraft and surface observations on CO2 flux estimation using an ensemble based 4-D data assimilation system, J. Geophys. Res., 116, D16306,doi:10.1029/2010JD015366, 2011.

Miyazaki, K., Eskes, H. J., Sudo, K., Takigawa, M., van Weele, M., and Boersma, K. F.: Simultaneous assimilation of satellite NO2, O3, CO, and HNO3 data for the analysis of tropospheric chemical composition and emissions, Atmos. Chem. Phys., 12, 9545-9579, https://doi.org/10.5194/acp-12-9545-2012 , 2012.

Miyazaki, K., Eskes, H. J., and Sudo, K.: A tropospheric chemistry reanalysis for the years 2005-2012 based on an assimilation of OMI, MLS, TES, and MOPITT satellite data, Atmos. Chem. Phys., 15, 8315-8348, https://doi.org/10.5194/acp-15-8315-2015, 2015.

Miyazaki, K., Bowman, K. W., Yumimoto, K., Walker, T., and Sudo, K.: Evaluation of a multi-model, multi-constituent assimilation framework for tropospheric chemical reanalysis, Atmos. Chem. Phys., 20, 931?967, https://doi.org/10.5194/acp-20-931-2020, 2020.

Mizzi, A. P., Arellano Jr., A. F., Edwards, D. P., Anderson, J. L., and Pfister, G. G.: Assimilating compact phase space retrievals of atmospheric composition with WRF-Chem/DART: a regional chemical transport/ensemble Kalman filter data assimilation system, Geosci. Model Dev., 9, 965?978, https://doi.org/10.5194/gmd-9-965-2016, 2016.

McTaggart-Cowan, R., and Zadra, A.: Representing Richardson Number Hysteresis in the NWP Boundary Layer, Mon. Wea. Rev., 143, 1232-1258, 2015.

Neish, M., Tanguay, M., Semeniuk, K., Polavarapu, S., DeGrandpre, J., Girard, C., Qaddouri, A., Gravel, S., Chan, D., Ren, S., GEM-MACH development team. (2019, June 19). GEM-MACH-GHG revision 137 (Version 137). Zenodo. http://doi.org/10.5281/zenodo.3246556

Palmer, P. I., D. J. Jacob, D. B. A. Jones, C. L. Heald, R. M. Yantosca, J. A. Logan, G. W. Sachse, and D. G. Streets, Inverting for emissions of carbon monoxide from Asia using aircraft observations over the western Pacific, J. Geophys. Res., 108(D21), 8828, doi:10.1029/2003JD003397, 2003.

Parrish, D.F. and Derber, J.C.: The National Meteorological Center's spectral statistical interpolation analysis system. Mon. Wea. Rev., 120, 1747-1763,1992.

Pavlovic, R., J. Chen, K. Anderson, M.D. Moran, P.-A. Beaulieu, D. Davignon, and S. Cousineau, 2016. The FireWork air quality forecast system with near-real-time biomass burning emissions: Recent developments and evaluation of performance for the 2015 North American wildfire season. J. Air & Waste Manage. Assoc., 66, 819-841, https://doi.org/10.1080/10962247.2016.1158214, 2016.

665 Polavarapu, S. M., Neish, M., Tanguay, M., Girard, C., de Grandpre, J., Semeniuk, K., Gravel, S., Ren, S., Roche, S., Chan, D., and Strong, K.: Greenhouse gas simulations with a coupled meteorological and transport model: the predictability of CO2, Atmos. Chem. Phys., 16, 12005-12038, https://doi.org/10.5194/acp-16-12005-2016, 2016.

Polavarapu, S. M., Deng, F., Byrne, B., Jones, D. B. A., and Neish, M.: A comparison of posterior atmospheric CO2 adjustments obtained from in situ and GOSAT constrained flux inversions, Atmos. Chem. Phys., 18, 12011-12044, https://doi.org/10.5194/acp-18-12011-2018,
670 2018.

Prive, N., Errico, R.M., and Carvalho, D. : Performance and evaluation of the Global Modeling and Assimilation Office observing system simulation experiment, 98th AMS annual Meeting, Austin, TX, 2018.

Spivakovsky, C. M., Logan, J. A., Montzka, S. A., Balkanski, Y. J., Foreman-Fowler, M., Jones, D. B. A., Horowitz, L. W., Fusco, A. C., Brenninkmeijer, C. A. M., Prather, M. J., Wofsy, S. C., and McElroy, M. B.: Three-dimensional climatological distribution of tropospheric
675 OH: Update and evaluation, Journal of Geophysical Research-Atmospheres, 105, 8931-8980, 2000.

van der Laan-Luijkx, I. T., et al. (2015), Response of the Amazon carbon balance to the 2010 drought derived with CarbonTracker South America, Global Biogeochem. Cycles, 29, 1092-1108, doi:10.1002/2014GB005082, 2015.

Voigt, C., Marushchak, M.E., Mastepanov, M., Lamprecht, R. E., Christensen, T. R., Dorodnikov, M., Jackowicz-Korczynski, M., Lindgren, A., Lohila, A., Nykanen, H., Oinonen, M., Oksanen, T., Palonen, V., Treat, C. C., Martikainen, P. J., and Biasi, C.: Ecosystem carbon
680 response of an Arctic peatland to simulated permafrost thaw. Glob Change Biol. 2019.

Wang, H., Jacob, D. J., Kopacz, M., Jones, D. B. A., Suntharalingam, P., Fisher, J. A., Nassar, R., Pawson, S., and Nielsen, J. E.: Error correlation between CO2 and CO as constraint for CO2 flux inversions using satellite data, Atmos. Chem. Phys., 9, 7313?7323, https://doi.org/10.5194/acp-9-7313-2009, 2009.

Worthy, D E., Platt, J. A., Kessler, R., Ernst, M., Audette , C., and Racki, S.: An update on the Canadian GHG measurement program,
685 In: Report of the 12th WMO/IAEA Meeting of Experts on Carbon Dioxide Concentration and Related Tracer Measurement Techniques, Toronto, Canada, September 2003, D. Worthy and L. Huang (editors), World Meteorological Organization Global Atmosphere Watch, Report 162, 220-231, 2005.

Yin, Y., F. Chevallier, P. Ciais, G. Broquet, A. Fortems-Cheiney, I. Pison, and M. Saunois : Decadal trends in global CO emissions as seen by MOPITT, Atmos. Chem. Phys., 15, 13,433-13,451, doi:10.5194/acp-15-13433-2015, 2015.